# Atmospheric Photo-Oxidation of 2-Ethoxyethanol: Autoxidation Chemistry of Glycol Ethers

Hongmin Yu, Kristian H. Møller, Reina S. Buenconsejo, John D. Crounse, Henrik G. Kjaergaard, and Paul O. Wennberg*

Read Online

**ABSTRACT:** We investigate the gas-phase photo-oxidation of 2-ethoxyethanol (2-EE) initiated by the OH radical with a focus on its autoxidation pathways. Gas-phase autoxidation—intramolecular H-shifts followed by $O_2$ addition—has recently been recognized as a major atmospheric chemical pathway that leads to the formation of highly oxygenated organic molecules (HOMs), which are important precursors for secondary organic aerosols (SOAs). Here, we examine the gas-phase oxidation pathways of 2-EE, a model compound for glycol ethers, an important class of volatile organic compounds (VOCs) used in volatile chemical products (VCPs). Both experimental and computational techniques are applied to analyze the photochemistry of the compound. We identify



oxidation products from both bimolecular and autoxidation reactions from chamber experiments at varied $HO_2$ levels and provide estimations of rate coefficients and product branching ratios for key reaction pathways. The H-shift processes of 2-EE peroxy radicals ($RO_2$) are found to be sufficiently fast to compete with bimolecular reactions under modest $NO/HO_2$ conditions. More than 30% of the produced $RO_2$ are expected to undergo at least one H-shift for conditions typical of modern summer urban atmosphere, where $RO_2$ bimolecular lifetime is becoming >10 s, which implies the potential for glycol ether oxidation to produce considerable amounts of HOMs at reduced $NO_x$ levels and elevated temperature. Understanding the gas-phase autoxidation of glycol ethers can help fill the knowledge gap in the formation of SOA derived from oxygenated VOCs emitted from VCP sources.
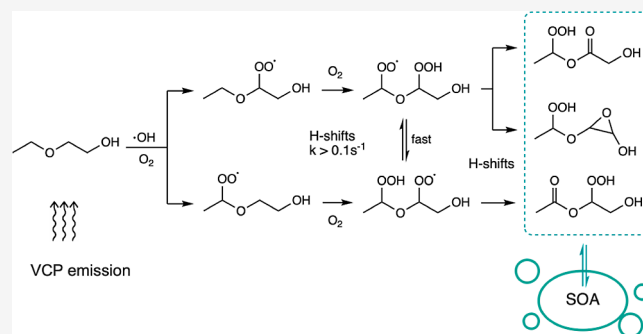
## 1. INTRODUCTION

The gas-phase oxidation of volatile organic compounds (VOCs) in the atmosphere is usually initiated by reactions with oxidative species such as OH, $NO_3$, and $O_3$. Subsequent addition of molecular oxygen ($O_2$) to the nascent alkyl radical leads to the formation of organic peroxy radicals ($RO_2$). The fate of $RO_2$ depends on the chemical state of the atmosphere, and traditionally, bimolecular reactions with NO, $HO_2$, or other $RO_2$ are considered to dominate their loss.[1,2] Recently, gas-phase autoxidation chemistry has been recognized to be another important pathway.[3−5] Autoxidation is generally defined as the process in which the $RO_2$ first undergoes an intramolecular hydrogen shift (H-shift), producing a hydroperoxyalkyl radical (often denoted QOOH in combustion chemistry), to which $O_2$ then rapidly attaches, forming a new, now more oxidized, $RO_2$. The successive isomerization and $O_2$ addition processes can result in rapid addition of oxygen to VOCs and, thereby, formation of highly oxygenated organic molecules (HOMs). HOMs have low volatility and thereby readily undergo gas-particle transfer, contributing to secondary organic aerosol (SOA) particle formation and/or growth.[3,6,7]

The autoxidation pathways become competitive with bimolecular chemistry as the bimolecular lifetime of $RO_2$

increases,[3,4,6,7] such as in environments with large emissions of VOCs and modest or low NO levels (0.1−1 ppb), where $RO_2$ can survive for 10−100 s before reacting with NO, $HO_2$, or other $RO_2$.[3,4] As a result of the recent successful reduction of $NO_x$ emission in urban areas (some urban $NO_x$ levels falling below 500 to 100 pptv[3,8]), autoxidation chemistry is expected to be increasingly favored in the photochemistry of a modern urban atmosphere. Given that autoxidation pathways can generate large amounts of low-volatility vapors that contribute to aerosol formation, it is imperative to characterize this low-$NO_x$ chemistry for the array of different VOCs typically found in an urban atmosphere.
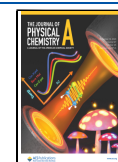
Success in air pollution control strategies can shift not only the major photochemical pathway of reactive organics in urban air but also the characteristics of these organic emissions. With VOC emission from combustion sources declining, volatile
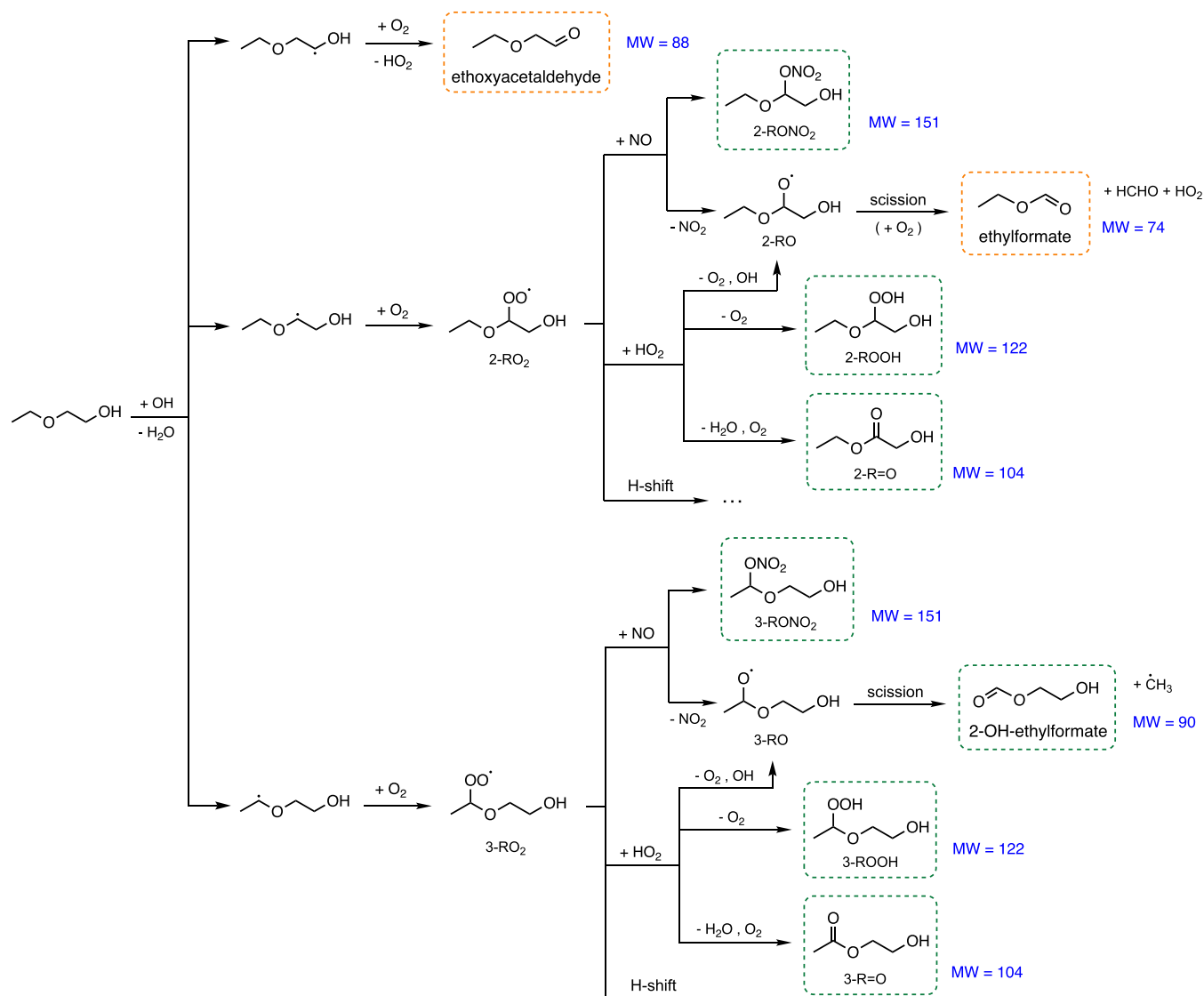
**Scheme 1. Oxidation of 2-EE by OH Radical[a]**



[a]H-abstraction from the methyl or hydroxy group is assumed to be negligible and is thus not shown. Subsequent reaction pathways of the peroxy radicals and some of the products are also shown, including $RO_2$ + NO reaction forming organonitrates ($RONO_2$) and alkoxy radicals (RO), $RO_2$ + $HO_2$ reaction forming hydroperoxides (ROOH), alkoxy radicals (RO), carbonyls (R=O), and unimolecular H-shifts. Major oxidation products are shown in boxes, with their molecular masses indicated in blue. Those that are detectable by our instrument are shown in green boxes, while those not detectable are shown in orange boxes.

chemical products (VCPs)—including solvents, personal care products, cleaning agents, coatings, etc.—have emerged as a new major source of VOC in industrialized cities.[9−11] VCPs are now considered to account for half or more of volatile organic emissions in some urban atmospheres and have been studied for their SOA forming potential under various conditions,[9−15] demonstrating that VCPs may account for much of the unexplained SOA mass in modern urban environments.[9,12] Since H-shift chemistry of $RO_2$ has been shown to be an important process for many organic substrates,[16−20] it is likely that many VCP compounds also produce HOMs via autoxidation.

In this study, we explore the gas-phase oxidation of 2-ethoxyethanol (2-EE, Scheme 1) as a model system for the diverse family of glycol ethers. Glycol ethers are compounds with formula of R-$(OCH_2CH_2)_n$-OR' ($n$ = 1, 2, and 3). They are a class of VCPs widely used as solvents in products such as

architecture coatings, cleaning products, and adhesives.[21−23] Studies have shown that many semi- or intermediate volatile glycol ether compounds are sufficiently volatile to evaporate and participate in atmospheric photochemical processes.[12,24] However, studies on photo-oxidation of glycol ethers remain sparse, and most still focus on traditional bimolecular pathways.[12,25,26] Here, we study 2-EE, the simplest glycol ether, as a model molecule of this class of compound. 2-EE is often used as a component or solvent for inks, paints, resins, dyes, and varnishes.[25] It is also detected in emissions from diesel/biodiesel blends used in vehicles.[27] We conduct a series of photo-oxidation experiments of 2-EE by OH radicals with differing $HO_2$ concentrations to explore the competition between bimolecular and autoxidation chemistry of 2-EE $RO_2$. Then, guided by computational techniques, we analyze the system to identify oxidation products and estimate the autoxidation rate coefficients.

**Scheme 2. Autoxidation Mechanism of the Peroxy Radicals in the 2-EE System based on Calculated H-Shift Rate Coefficients at 298.15 K[a]**
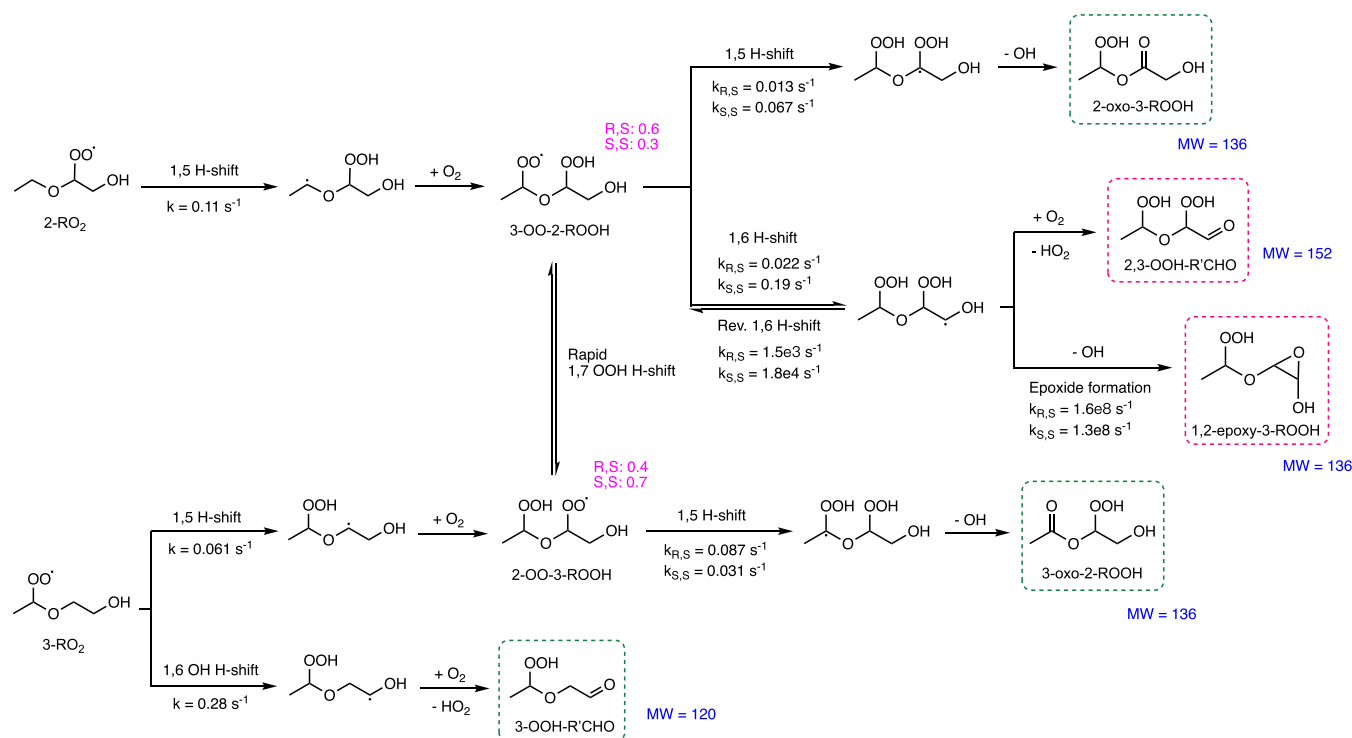


[a]Rate coefficients for different diastereomers of radicals are indicated separately. Here, we refer to the diastereomers with the same configuration at both chiral centers as (S, S) [including (R, R) and (S, S) isomers] and those with different configuration as (R, S) [including (S, R) and (R, S) isomers]. The fast 1,7 OOH H-shift between peroxy radicals 3-OO-2-ROOH and 2-OO-3-ROOH establishes an equilibrium between the two radicals. The calculated relative abundance of diastereomers of 3-OO-2-ROOH and 2-OO-3-ROOH at equilibrium is indicated in pink. The products that are detectable by our instrument are shown in green boxes. The products that are not detected in our experiments are shown in pink boxes.

## 2. METHODS

**2.1. Experimental Design.** We conduct a suite of oxidation experiments of 2-EE (Sigma-Aldrich, >99%) initiated by the reaction with the OH radical at different $HO_2$ mixing ratios in a ~ 0.7 m$^3$ Teflon environmental chamber. The chamber is housed inside an enclosure with UV reflective metal and can be equipped with either 350 nm (Sylvania 350 Blacklight) or 254 nm (Sankyo Denki G40T10) UV lamps. Experiments are conducted under laboratory temperature at 294 ± 1 K and pressure at ~993 hPa, and under high temperature at 309.5 ± 2 K with a heater (Finlandia FIN-45) being used to warm the chamber enclosure. The mechanism of 2-EE oxidation by OH radical is shown in Scheme 1. Two major peroxy radicals (2-RO$_2$ and 3-RO$_2$, Scheme 1) are produced through the initiation step.

To constrain the H-shift rate coefficients of RO$_2$ in the system, we study the competition between the RO$_2$ + HO$_2$ bimolecular channel and autoxidation chemistry by comparing the yields of hydroperoxides, the major products from the RO$_2$ + HO$_2$ channel, and autoxidation products as HO$_2$ concentrations are varied. The RO$_2$ in the system is prepared by oxidation of 2-EE via OH radicals, which are produced from photolysis of H$_2$O$_2$ (30% by mass, Macron Fine Chemicals) through reaction

$$H_2O_2 \xrightarrow{h\nu} 2OH \tag{R1}$$

Most of the HO$_2$ is formed in the chamber by addition of CH$_3$OH (Sigma-Aldrich, >99.9%) resulting in

$$CH_3OH + OH \xrightarrow{O_2} HO_2 + HCHO + H_2O \tag{R2}$$

A small additional amount of HO$_2$ is produced via the reaction of OH with H$_2$O$_2$, via the reactions following alkoxy formation, and in several of the autoxidation channels.

To study the rate of unimolecular chemistry, we performed experiments at variable concentrations of HO$_2$. We vary HO$_2$ concentrations across different experiments by changing the number and the type of UV lamp in the chamber enclosure, thereby modifying the production rate of OH (reaction R1) and subsequently the production of HO$_2$ (reaction R2). We keep the oxidation rate of CH$_3$OH much higher than that of 2-EE, to not only ensure that the production rate of HO$_2$ greatly exceeds that of RO$_2$ so that RO$_2$ + RO$_2$ chemistry is minimized but also help constrain the HO$_2$ concentrations in the chamber. A detailed description about the method determining [HO$_2$] in our system is given in Section S6.1. In our experiments, the CH$_3$OH concentrations are ~46 ppm (~1.1 × 10$^{15}$ mol/cm$^3$), and 2-EE concentrations are ~600 ppb (~1.5 × 10$^{13}$ mol/cm$^3$) (see Table S1 for a list of experimental conditions). The resulting [HO$_2$] ranges from ~1.7 × 10$^9$ mol/cm$^3$ (~0.07 ppb) with one 350 nm UV light, to ~6.2 × 10$^{10}$ mol/cm$^3$ (~2.5 ppb) with eight 254 nm UV lights. Estimates of the concentration of [HO$_2$] in each experiment are determined using the box model described below and are listed in Table S9 in Section S5.

In most experiments, we infer the amount of 2-EE oxidized (Δ[2-EE]) during the experiment by the addition of ethylene glycol (EG, HOCH$_2$CH$_2$OH, Sigma-Aldrich, 99.8%), measur-

ing its decay and the growth of its major oxidation product glycoaldehyde ($HOCH_2CHO$, formed through the reaction: $HOCH_2CH_2OH + OH \xrightarrow{O_2} HOCH_2CHO + H_2O + HO_2$). The rate coefficient for the reaction of OH with EG at room temperature is measured by Aschmann and Atkinson[28] to be $(1.47 \pm 0.26) \times 10^{-11}$ cm$^3$ mol$^{-1}$ s$^{-1}$. A more detailed description of determining $\Delta[2\text{-EE}]$ is given in Section S6.3.

**2.2. Instrumentation.** The oxidation products are measured by a low-pressure gas chromatography technique combined with high-resolution time-of-flight chemical ionization mass spectrometry (GC-CIMS) using $CF_3O^-$ as a reagent ion. The configuration of the instrument is described in detailed elsewhere,[3,29,30] and a brief summary is provided here. The GC-CIMS technique was developed to provide isomer-resolved detection of gas-phase oxygenated organic compounds, including many species that are traditionally deemed difficult to measure, e.g., organic hydroperoxides and nitrates. However, products with low volatility that would readily partition into a condensed phase may fail to be detected in our experiments despite being sensitive to the instrument. The GC consists of a 1 m fused silica column (Restek RTX-1701), which is cooled through evaporation and expansion of liquid $CO_2$ and warmed up by an electrical heating system, with nitrogen served as the carrier gas. The mass spectrometer (HRToF-CIMS) can sample either from the output of GC (GC mode) or directly from the chamber (direct sampling mode). In the GC mode, the oxidation products are first cryotrapped and preconcentrated at the head of the GC column and then separated as column temperature increases at a predetermined ramp rate controlled by an automated temperature program. After eluting from the GC column, the analytes are transferred to the CIMS and react with $CF_3O^-$ through simple clustering chemistry and are observed as $CF_3O^-$ cluster ions at $m/z$ neutral mass +85 amu.[29] Quantification of the analytes requires knowledge of the CIMS sensitivity of the target compound, which for well-bound clusters is proportional to their ion−molecule collision rate with $CF_3O^-$. The ion−molecule collision rate is determined by methods in a study by Su and Chesnavich[31] using the calculated dipole moment and polarizability of the molecule.[32] We estimated instrumental sensitivity for major products observed in the system based on the ion−molecule collision rate and measured sensitivity for EG.[33] The resulting sensitivities are shown in Table S5 in Section S3, along with a more detailed description of the CIMS calibration processes and the calculated dipole moments, polarizabilities, and ion−molecule collision rates of the oxidation products.

**2.3. Computational Method.** We calculate the rate coefficients of the H-shift reactions of key radicals in the system using multiconformer transition state theory (MC-TST)[34] following the approach detailed by Møller et al.[35] This approach has continually yielded unimolecular $RO_2$ reaction rate coefficients within a factor of 5 of experimentally available values and has recently been extended to alkoxy radical unimolecular reactions.[35−38] The computational results guide the development of the autoxidation mechanism for 2-EE illustrated in Scheme 2 and subsequent schemes. We calculate the rate coefficients of all potentially competitive H-shifts of the peroxy radicals but only include those with appreciable rates ($>10^{-4}$ s$^{-1}$) in our schemes and following analysis.

Conformers of the reactant and transition state (TS) are sampled systematically using MMFF[39] in Spartan'14 (Wavefunction, Inc.) with constraints on selected bond lengths in the

TS geometry and forcing a neutral charge on the radical center. The resulting structures are optimized at the B3LYP/6-31+G(d) level in Gaussian 16, Revision C.01 (Gaussian, Inc.) with an optimization with the selected bond lengths constrained preceding the free TS optimization for the TSs.[40,41] Unique conformers with electronic energies within 2 kcal/mol of the lowest-energy conformer further undergo an optimization and frequency calculation at the $\omega$B97X-D/aug-cc-pVTZ level.[42] For the lowest-energy conformer of the reactant and TS, a CCSD(T)-F12a/VDZ-F12 single-point energy calculation is carried out in MOLPRO 2012.1 for more accurate barrier heights.[43,44] This final single-point calculation is omitted for the alkoxy radicals. Tunneling coefficients are calculated using the 1D Eckart approach based on IRC end-point calculated at the same theoretical level as the barrier heights.[45]

MC-TST reaction rate coefficients, $k$, are then calculated as

$$ k = \kappa \frac{k_B T}{h} \frac{\sum_i^{TS} \exp\left(\frac{-\Delta E_i}{k_B T}\right) Q_{TS_i}}{\sum_j^{R} \exp\left(\frac{-\Delta E_j}{k_B T}\right) Q_{R_j}} \exp\left(-\frac{E_{TS} - E_R}{k_B T}\right) \quad (1) $$

where $\kappa$ is the Eckart tunneling coefficient, $k_B$ is the Boltzmann constant, $T$ is the absolute temperature, and $h$ is Planck's constant. The sum in the numerator sums the rigid-rotor harmonic oscillator partition functions of all included TS conformers, each exponentially weighted by their relative ZPVE-corrected energy. The sum in the denominator is the same for the reactant conformers. The partition functions and relative energies are calculated at the $\omega$B97X-D/aug-cc-pVTZ level. The final exponential term is the energy difference between the lowest-energy reactant and TS conformers with electronic energies at the CCSD(T)-F12a/VDZ-F12 level and ZPVE at the $\omega$B97X-D/aug-cc-pVTZ level. For the alkoxy reactions, the electronic energy is also calculated at the $\omega$B97X-D/aug-cc-pVTZ level.

**2.4. Box Model.** We use a MATLAB-based gas-phase chemistry box model to simulate our experiments and, by comparison with the experimental results, evaluate the kinetics and branching ratios of the chemistry. The model uses a MATLAB ode15s solver to calculate time-dependent concentrations of species in the system based on the given initial conditions and a given chemical mechanism. Initially, the reactions and kinetic data implemented in the model are adopted from the Master Chemical Mechanism (MCM, https://mcm.york.ac.uk/MCM), estimation from Jenkin et al.,[46] and the calculated H-shift rates. Further details regarding the oxidation mechanism and reaction kinetics we used in the model are given in Section S1. We then minimize the difference between the chamber data and the simulations by adjusting the $RO_2$ H-shift rates and branching fractions of bimolecular reactions in the mechanism within their calculated uncertainties. The rate coefficients of $RO_2$ bimolecular reactions, calculated rate coefficients of alkoxy radical unimolecular reactions, and the rapid equilibrium between 3-OO-2-ROOH and 2-OO-3-ROOH (see Scheme 2) are not altered.

## 3. RESULTS AND DISCUSSION

In our analysis, we seek to generate a nearly complete chemical mechanism for the oxidation of 2-EE by OH to the first-generation closed-shell products. We use the bimolecular chemistry reported in the literature and MCM as our prior,[46−49] along with the H-shift chemistry from our calculations. We then modified the mechanism by adjusting
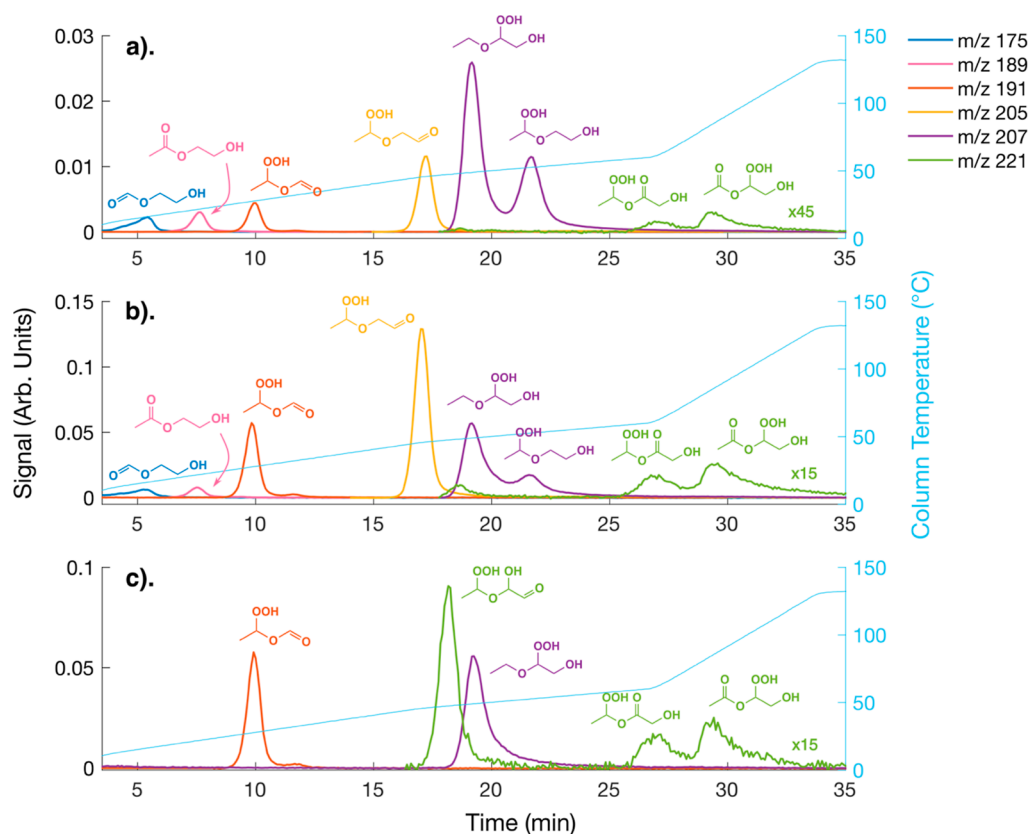
**Figure 1.** Gas chromatograms of major oxidation products from $HO_2$ experiments, including 2-OH-ethylformate ($m/z$ 175), 3-R═O ($m/z$ 189), 3-OOH-R′═O ($m/z$ 191), 3-OOH-R′CHO ($m/z$ 205), ROOH's (2-ROOH and 3-ROOH, $m/z$ 207), and oxo-ROOH's (2-OH-3-OOH-R′CHO, 2-oxo-3-ROOH, 3-oxo-2-ROOH, $m/z$ 221). (a) 2-EE high $HO_2$ experiment with $[HO_2] = 3.4 \times 10^{10}$ mol/cm$^3$ (1.38 ppb), (b) 2-EE low $HO_2$ experiment with $[HO_2] = 5.1 \times 10^9$ mol/cm$^3$ (0.21 ppb), and (c) experiment with EVE. The $m/z$ 221 signals are scaled up by a factor denoted in the figure.

## Scheme 3. Oxidation of Ethyl Vinyl Ether (EVE) by the OH Radical[a]
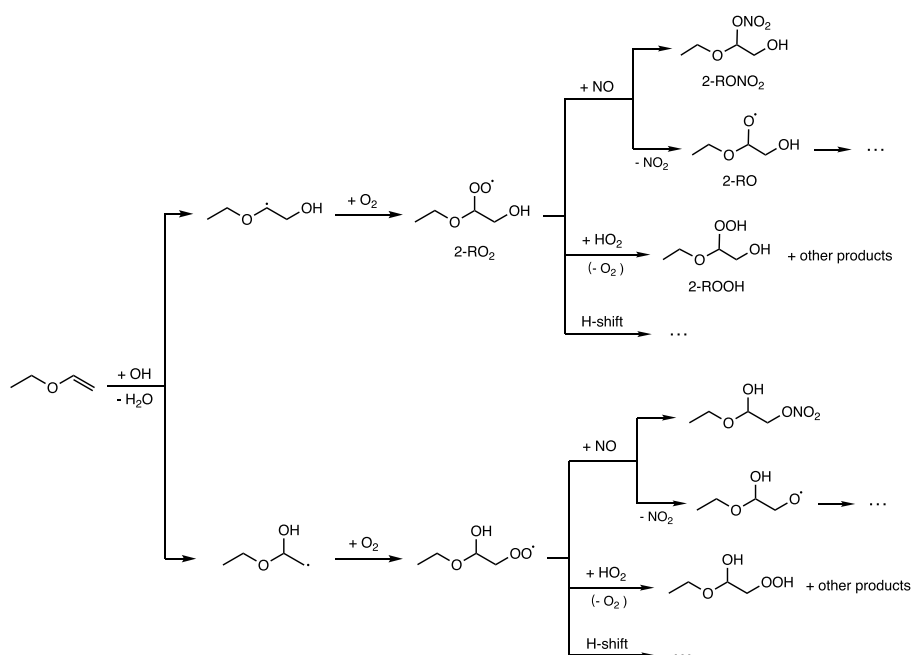


[a]The branching ratio of OH addition at primary carbon to secondary carbon for 1-alkene is estimated to be 0.65:0.35.[50]

the branching ratios of relevant reactions and H-shift rates to best match the observed dependence of the closed shell products on the abundance of $HO_2$. Optimization of the mechanism is achieved through the following steps: (1). using prior

**Scheme 4. Bimolecular Pathways of Peroxy Radicals 3-OO-2-ROOH and 2-OO-3-ROOH Based on Calculated Rate Coefficients at 298.15 K[a]**
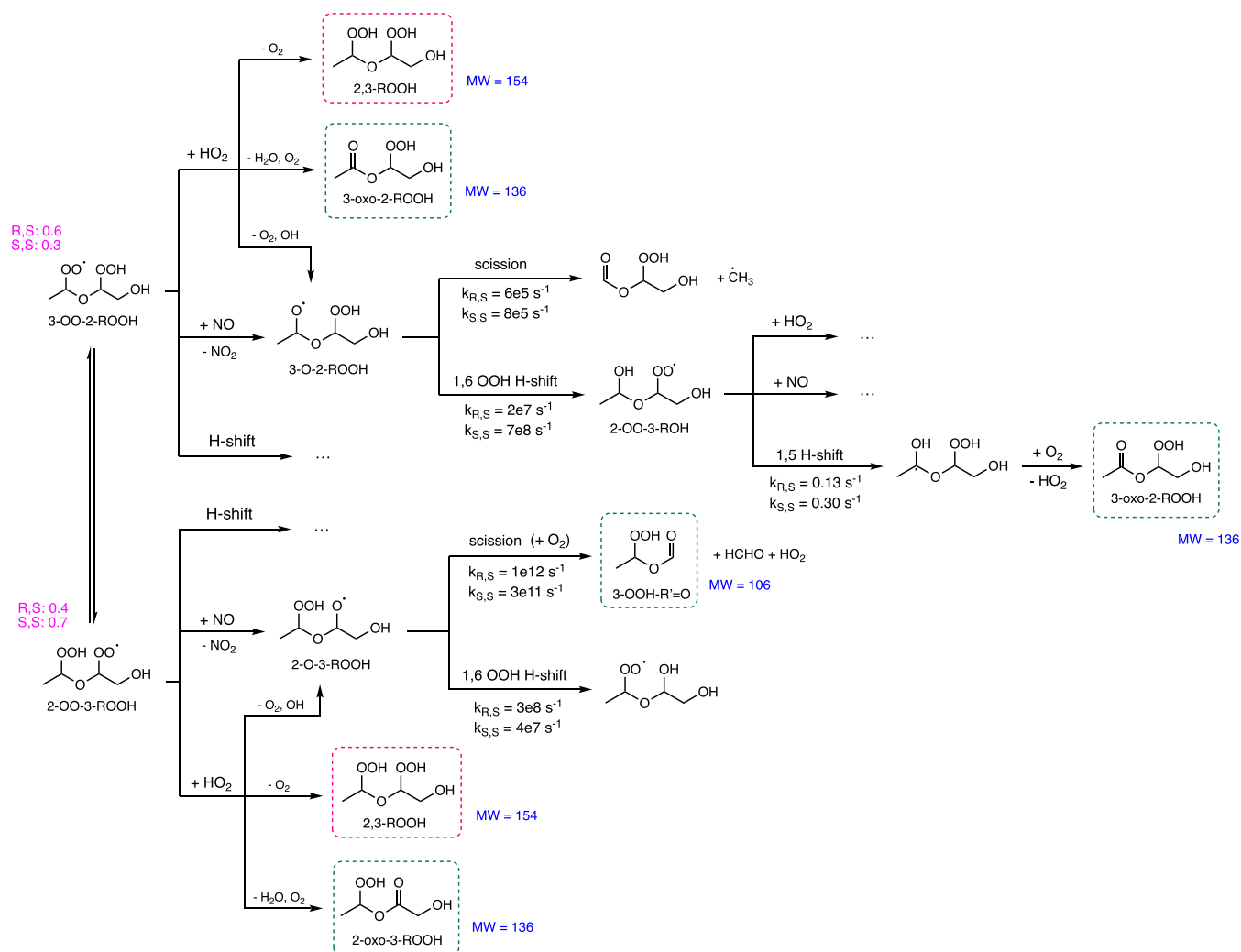


[a]The products that are detectable by our instrument are shown in green boxes, and those not detected in our experiments are shown in pink boxes.

information and gas-phase synthesis of standards to assign the observed signals in the gas chromatogram (based on their molecular weight and elution temperature) to the expected products in the 2-EE oxidation mechanism (Section 3.1); (2). using the observed ratio between major products from $RO_2$ + $HO_2$ reactions to infer the branching ratios for the bimolecular pathway (Section 3.2.1) and the location of hydrogen abstraction from 2-EE (Section 3.2.3); and (3). estimating H-shift rates for various $RO_2$ in the mechanism based on the variation in the measured yields of relevant oxidation products at different $[HO_2]$ (Sections 3.2.2−2.5).

## 3.1. Identity of Oxidation Products from Experiments with $HO_2$.

Figure 1 shows the gas chromatograms of major 2-EE oxidation products formed in an experiment under high $[HO_2]$ ($3.4 \times 10^{10}$ mol/cm$^3$) and an experiment under low $[HO_2]$ ($5.1 \times 10^9$ mol/cm$^3$), corresponding to $RO_2$ lifetimes of approximately 2 and 12 s, respectively. Figure 1c also shows the products formed in the OH-initiated oxidation of ethyl vinyl ether (EVE, Sigma-Aldrich, ≥99%) to assist in identifying the structural isomers. Scheme 3 shows the mechanism of EVE oxidation by OH. The major pathway for OH addition to 1-alkene compounds[50] produces the same 2-$RO_2$ as in 2-EE

oxidation, allowing us to confirm the identification of products from 2- and 3-$RO_2$ channels in 2-EE oxidation. The oxidation experiments of EVE are conducted in the same manner as the 2-EE experiments except that we increase the amount of $CH_3OH$ used to keep the ratio of $HO_2$ to $RO_2$ production rates similar.

Oxidation products of interest in Figure 1 include 2-OH-ethylformate ($m/z$ 175), 3-R═O ($m/z$ 189), and the hydroperoxides (ROOHs, $m/z$ 207), which are products from the bimolecular $RO_2$ + $HO_2$ channel with higher yields at higher $HO_2$ condition; 3-OOH-R'CHO ($m/z$ 205) produced via H-shift chemistry from 3-$RO_2$, and the ketohydroperoxides (oxo-ROOH's, $m/z$ 221) produced from both 2- and 3-$RO_2$ H-shift chemistry, both of which have higher yields at lower $HO_2$ condition.

We identify the $m/z$ 191 peak eluting at ∼10 min as 3-OOH-R'═O ($m/z$ 191) through deuterium exchange experiments to eliminate from consideration the exact mass isomers, e.g., the diols (2-ROH and 3-ROH) produced from self-reactions of 2- and 3-$RO_2$ (Scheme S2). Details about the deuteration experiment are described in Section S7.1. 3-OOH-R'═O is formed following an alkoxy bond scission in the bimolecular chemistry of the 2-OO-3-ROOH peroxy radical, as shown in

Scheme 4. The high yield of this product under elevated $HO_2$ levels suggests that the reaction of 2-OO-3-ROOH with $HO_2$ has a large yield of the 2-O-3-ROOH alkoxy radical, similar to the reactions of other highly functionalized $RO_2$.[51,52] The compound is also observed in EVE experiments (Figure 1c), which demonstrates the production of 2-OO-3-ROOH from 2-$RO_2$, likely through rapid equilibrium between 3-OO-ROOH and 2-OO-3-ROOH radicals (Schemes 2 and 4). Such a rapid H-shift between ROOH and $RO_2$ is also observed in other aliphatic and acyl peroxy radicals.[53−55]

To assign the GC signals at $m/z$ 221, we oxidized ethyl glycolate (2-R=O in Scheme 1, Sigma-Aldrich, 98%) and 2-hydroxyethyl acetate (3-R=O in Scheme 1, TCI, >60%) under high $HO_2$ condition to produce 2-oxo-3-ROOH and 3-oxo-2-ROOH in the system (oxidation mechanism in Scheme 5). The

**Scheme 5. Oxidation of Ethyl Glycolate (2-R=O) and 2-Hydroxyethyl Acetate (3-R=O) by OH under High $HO_2$ Condition**
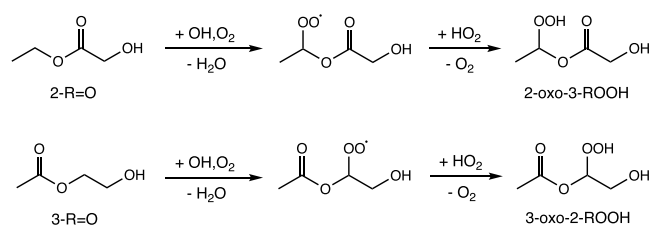


resulting gas chromatograms at $m/z$ 189 and $m/z$ 221 from the experiments are shown in Figure S2 in Section S7.1. Comparing with the peaks at the same $m/z$ from a 2-EE and an EVE experiment, we identify the two $m/z$ 221 peaks eluting at higher temperature. We speculate that the first GC peak at $m/z$ 221 corresponds to the compound that we denote as 2-OH-3-OOH-R'CHO (Figure 1). We propose a formation mechanism of this compound in Scheme 6. In the EVE system, it is likely formed through consecutive H-shift processes. In the 2-EE system, we speculate that it is produced from heterogeneous chemistry of the 1,2-epoxy-3-ROOH. We hypothesize that the epoxide undergoes acid-catalyzed ring-opening reactions on the chamber walls or in the CIMS instrument.[56,57] The observation of 2-OH-3-OOH-R'CHO likely indicates the formation of 1,2-epoxy-3-ROOH as predicted by theory (Scheme 2). The

possibility for glycol ethers to form gas-phase epoxides suggests a route to formation of SOA, as such epoxides are known to be SOA precursors.[58,59] The reactive uptake and ring-opening of gas-phase hydroxy-substituted epoxides on surfaces have been demonstrated to be a major pathway that leads to SOA formation under low $NO_x$ conditions.[56,58−60]

## 3.2. Products Branching Ratios and H-Shift Rate Coefficients.
The following sections describe our estimation of the branching ratios of several reaction pathways and the $RO_2$ H-shift rate coefficients in the 2-EE photo-oxidation mechanism. For each of these parameters, we also evaluate their variation with temperature by performing experiments under similar initial conditions at higher temperature of 309.5 ± 2 K. At elevated temperature, H-shift rates of $RO_2$ increase due to the high energy barrier along the H-shift reaction coordinate,[3,6,52] while the bimolecular rate coefficients between $RO_2$ and $HO_2$ are expected to be slightly slower.

*3.2.1. Branching Ratios for the $RO_2$ + $HO_2$ Reaction.* We estimate the product branching ratios of reaction channels for reactions of 2-EE peroxy radicals with $HO_2$ by quantifying the closed-shell products of the bimolecular pathways. Reactions between $HO_2$ and peroxy radicals 2-$RO_2$ and 3-$RO_2$ are expected to form hydroperoxides (2-ROOH and 3-ROOH), carbonyls (2-R=O and 3-R=O), alkoxy radicals (2-RO and 3-RO), and their subsequent products (pathways a, b, and c for Reactions 3 and 4 in Scheme 7). Most products from the 3-$RO_2$ + $HO_2$ reaction form stable clusters with $CF_3O^-$, while from the 2-$RO_2$ + $HO_2$ reaction, 2-ROOH is the only product that is quantifiable (detection of 2-R=O is discussed in Section S7.1). Thus, we use the measured yields of major 3-$RO_2$ + $HO_2$ reaction products, i.e., 3-ROOH, 3-R=O, and 2-OH-ethyl-formate, to infer products branching ratios of $RO_2$ + $HO_2$ reactions in the 2-EE system. In the absence of secondary chemistry, the ratio of yields of the products should be equivalent to the ratio of their production. To derive a more accurate ratio of product yields, concentrations of the products (used in the analysis in the following sections) are corrected by accounting for their secondary losses. The detailed procedure of data correction and potential biases in the procedure are described in Section S4.

Figure 2 shows the concentrations of 3-R=O and 2-OH-ethylformate as a function of the concentration of 3-ROOH. At 294 K, the yield of 3-R=O relative to that of 3-ROOH is measured to be 0.059 ± 0.017, and the yield of 2-OH-

**Scheme 6. Speculative Formation Pathways of 2-OH-3-OOH-R'CHO from (a) 2-EE and (b) EVE[a]**
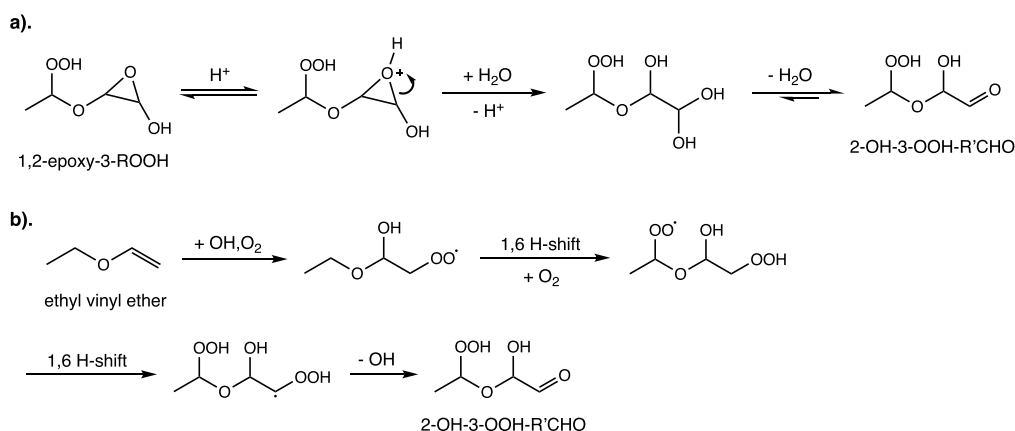


[a]The mechanism for 2-EE may occur heterogeneously on the chamber walls or in the CIMS instrument.

## Scheme 7. Mechanism of 2-RO$_2$ + HO$_2$ (3a−3c) and 3-RO$_2$ + HO$_2$ (4a−4c) Reactions[a]
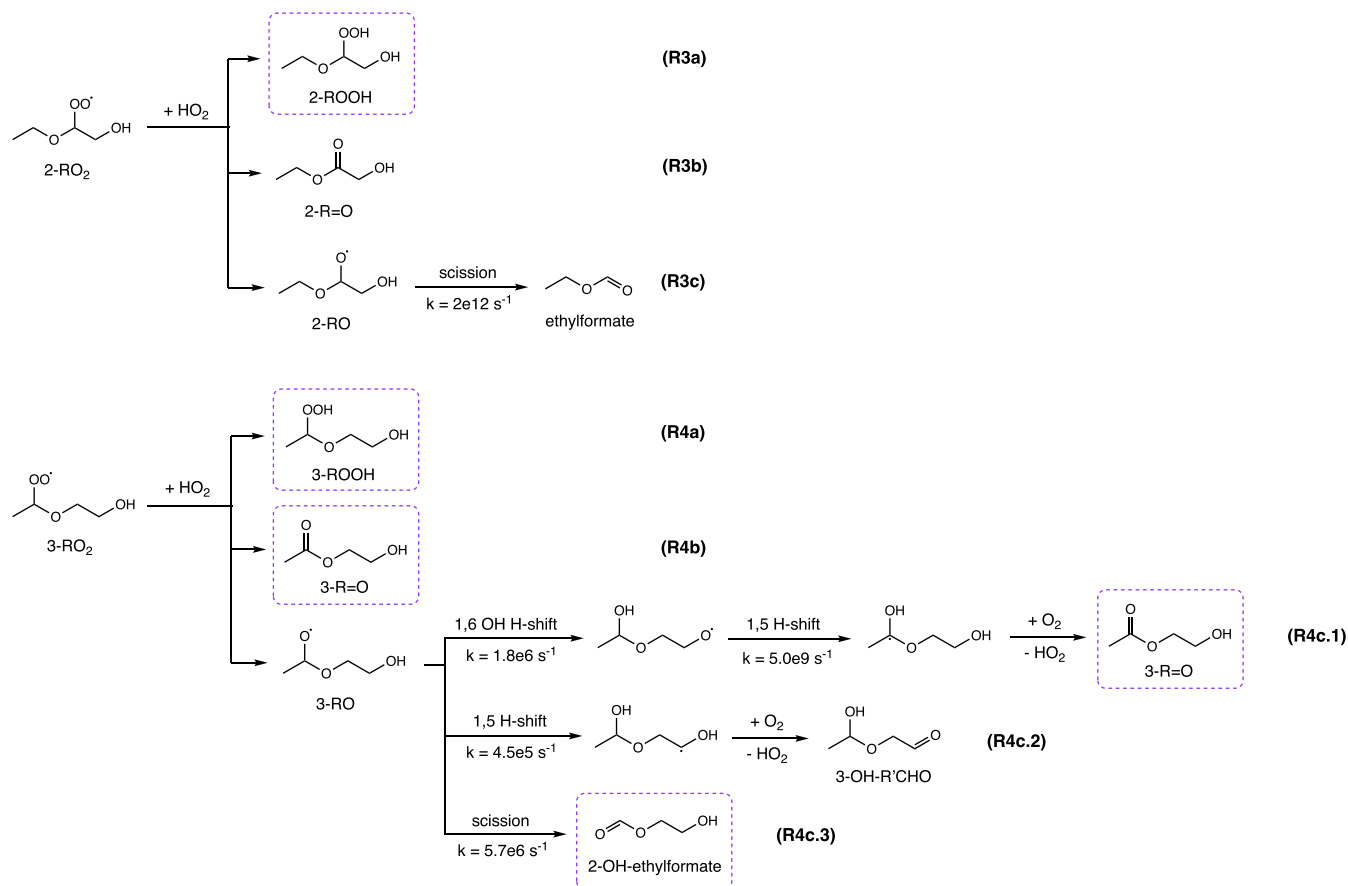


[a]Products quantifiable are highlighted in purple boxes. Rate coefficients for isomerization and decomposition of alkoxy radicals are calculated at 298.15 K using the MC-TST method.[38] Calculated MC-TST alkoxy rate coefficients have uncertainties likely within a factor of 10. For the co-products and reagents in each pathway, refer to Schemes 1 and S1.
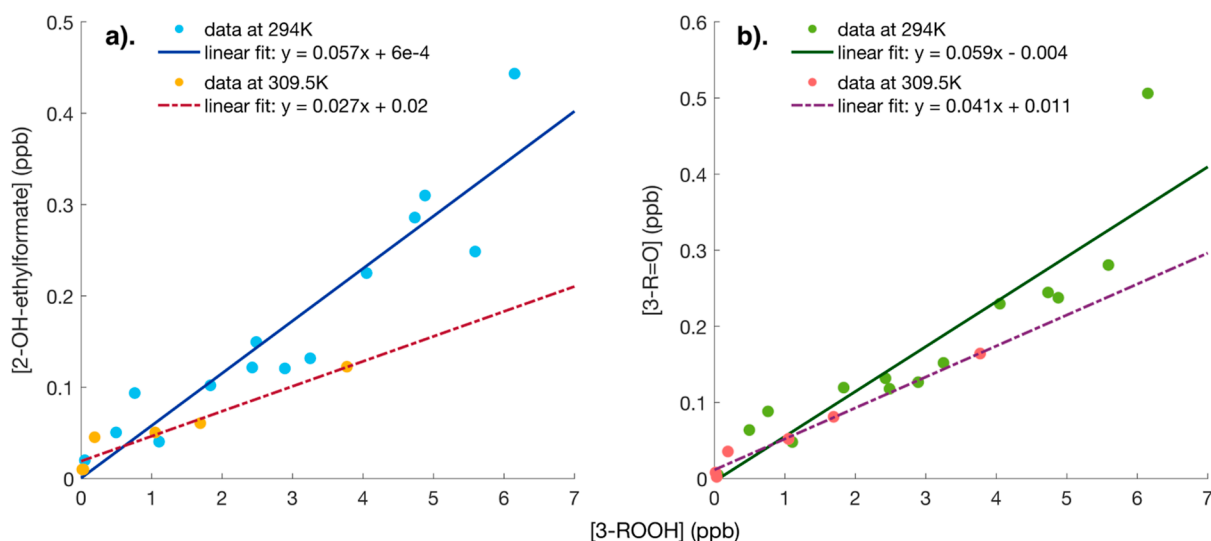


**Figure 2.** (a) [2-OH-ethylformate] vs [3-ROOH] and (b) [3-R═O] vs [3-ROOH] at ambient temperature (294 K) and high temperature (309.5 K). Solid lines are unweighted linear regression fits to ambient temperature data, and dashed lines are unweighted linear regression fits to high-temperature data. The uncertainties in the data are mainly systematic (∼21%) due to knowledge of the instrumental calibration detailed in Section S6. Respective $R^2$ values of the linear fits are 0.87 (blue solid line), 0.92 (red dashed line), 0.83 (green solid line), and 0.97 (purple dashed line).

ethylformate relative to that of 3-ROOH is 0.057 ± 0.016. At 309.5 K, the yield of 3-R═O relative to that of 3-ROOH is 0.041

± 0.011, and the yield of 2-OH-ethylformate relative to that of 3-ROOH is 0.027 ± 0.008.

Since 3-R=O is produced both directly from 3-RO$_2$ + HO$_2$ (reaction 4b) and from isomerization of the 3-RO radical (reaction 4c.1), deriving product branching ratios of the 3-RO$_2$ + HO$_2$ reaction also requires knowledge of branching fractions of 3-RO unimolecular pathways. We investigate 3-RO chemistry by conducting a few experiments of 2-EE with NO, in which the production and reaction of alkoxy radicals are dominant. In these experiments, H$_2$O$_2$ still serves as the source of OH radicals, and NO (sourced from cylinder containing 1993 ± 20 ppmv in N$_2$, Matheson) is added instead of CH$_3$OH as the source of bimolecular reactants. The gas chromatograms and analysis of the results from NO experiments are given in Section S7.2. As shown in the chromatograms in Figure S3a, we observe high yields of decomposition products 2-OH-ethylformate ($m/z$ 175), smaller yields of 3-R=O ($m/z$ 189) from isomerization pathway R4c.1, and probably minimal amounts of 3-OH-R'CHO ($m/z$ 189) from the isomerization pathway R4c.2. The measured concentrations of 3-R=O (possibly together with 3-OH-R'CHO) and 2-OH-ethylformate suggest that the ratio of their production is around 0.095 ± 0.024 (Figure S5). Thus, we suggest that the ratio between isomerization and decomposition channels (($k_{4c.1}$ + $k_{4c.2}$)/$k_{4c.3}$) of 3-RO is ~1/10. Our finding that 2-OH-ethylformate is the dominant product of the unimolecular reactions of this alkoxy radical agrees with our MC-TST calculations, and this inferred branching ratio is well within the uncertainty of the computational prediction for alkoxy radical unimolecular reactions.[38]

Given that there are still uncertainties in our understanding of the effect of chemical activation and temperature on the ratio between isomerization and decomposition channels of alkoxy radicals,[61,62] here we assume that the 1:10 ratio of ($k_{4c.1}$ + $k_{4c.2}$):$k_{4c.3}$ also applies to 3-RO produced from HO$_2$ experiments and at elevated temperature. With this assumption, the branching fractions for the 3-RO$_2$ + HO$_2$ reaction pathways are listed in Table 1. We apply the resulting branching ratios in the box model for both the 3-RO$_2$ + HO$_2$ and 2-RO$_2$ + HO$_2$ reactions.

**Table 1. Branching Ratios for Reaction Channels (4a–4c) for the 3-RO$_2$ + HO$_2$ Reaction Estimated from the Observed Product Yields[a]**

| reaction channels | branching ratios at 294 K | branching ratios at 309.5 K |
|---|---|---|
| $k_{4a}/k_4$ | 0.896 ± 0.026 | 0.936 ± 0.016 |
| $k_{4b}/k_4$ | 0.048 ± 0.013 | 0.035 ± 0.009 |
| ($k_{4c.1}$ + $k_{4c.2}$)/$k_4$ | 0.005 ± 0.002 | 0.003 ± 0.001 |
| $k_{4c.3}/k_4$ | 0.051 ± 0.014 | 0.026 ± 0.008 |

[a]Derivation of the uncertainties is detailed in Section S6.

**3.2.2. 1,6 H-Shift Rate of 3-RO$_2$.** We estimate the 1,6 H-shift rate of 3-RO$_2$ (which leads to the formation of the hydroperoxyl aldehyde, 3-OOH-R'CHO, Scheme 2) from the variation in the yields of 3-ROOH and 3-OOH-R'CHO at different [HO$_2$]. The ratio of the yields of the two products is equivalent to the ratio between their formation rates

$$\frac{[3\text{-ROOH}]}{[3\text{-OOH-R'CHO}]}$$
$$= \frac{\alpha_{4a}k_{RO_2+HO_2}[3\text{-RO}_2][HO_2]}{k_{1,6H\text{-shift},3\text{-RO}_2}[3\text{-RO}_2]}$$
$$= \frac{\alpha_{4a}k_{RO_2+HO_2}}{k_{1,6H\text{-shift},3\text{-RO}_2}}[HO_2]$$

$$(2)$$

where $\alpha_{4a}$ indicates the branching fraction to ROOH formation derived in the previous section. Thus, the ratio between the yields of 3-ROOH and 3-OOH-R'CHO is expected to be proportional to [HO$_2$]. As illustrated in Figure 3, we observe a
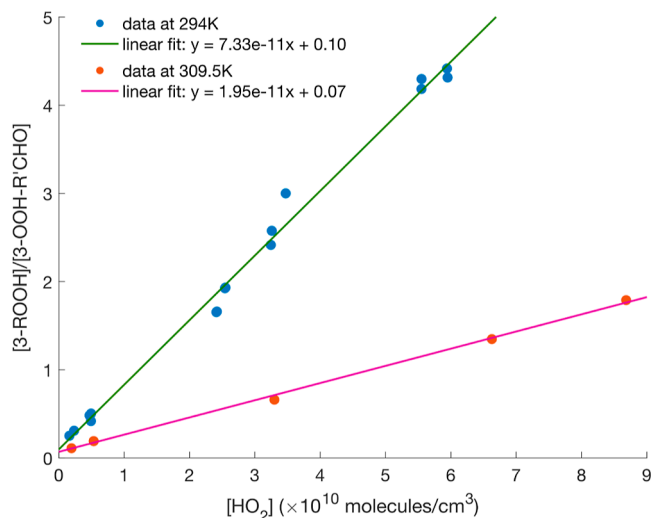


**Figure 3.** [3-ROOH]/[3-OOH-R'CHO] vs [HO$_2$] at ambient temperature (294 K) and high temperature (309.5 K) and respective unweighted linear regression fits. The uncertainties in the data are mainly systematic and are detailed in Section S6 (~25% for concentration ratios and ~17% for [HO$_2$]). The respective $R^2$ values of the linear fits are 0.992 for ambient temperature data (green solid line) and 0.998 for high-temperature data (pink solid line).

linear relationship between the ratio of product yields to [HO$_2$] at both ambient and elevated temperature. The slope is equal to the ratio between the bimolecular rate coefficient (with the branching to hydroperoxides $\alpha_{4a}$) and the unimolecular H-shift rate coefficient $\left(\frac{\alpha_{4a}k_{RO_2+HO_2}}{k_{1,6H\text{-shift},3\text{-RO}_2}}\right)$.
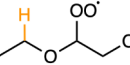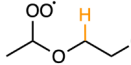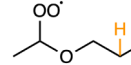
As shown in Figure 3, the slope is nearly four times smaller at high temperature, consistent with a much higher H-shift rate and a higher yield of the autoxidation product at elevated temperatures. From the linear regression fitting, we derive the ratio of $\frac{\alpha_{4a}k_{RO_2+HO_2}}{k_{1,6H\text{-shift},3\text{-RO}_2}}$ at ambient temperature to be (7.33 ± 2.21) × 10$^{-11}$ cm$^3$ mol$^{-1}$ and at high temperature to be (1.95 ± 0.59) × 10$^{-11}$ cm$^3$ mol$^{-1}$. We evaluate the bimolecular rate coefficient of RO$_2$ + HO$_2$ reaction based on derivations from Wennberg et al.[19] and Jenkin et al.[46] Along with our derivation of the branching fractions of ROOH formation from the previous section, we estimate the 1,6 H-shift rate coefficient of 3-RO$_2$ to be 0.21 ± 0.13 s$^{-1}$ at 294 K, and 0.67 ± 0.42 s$^{-1}$ at 309.5 K. Both values agree well with computational prediction of the rate coefficient (0.21 and 0.57 s$^{-1}$ respectively, uncertainty within a factor of 5). This estimated H-shift rate increases by approximately a factor of 3 when the temperature increases by ~15 K.

**3.2.3. 1,5 H-Shift Rates of 2- and 3-RO$_2$.** 1,5 H-shifts of 2- and 3-RO$_2$ lead to the formation of peroxy radicals 3-OO-2-ROOH and 2-OO-3-ROOH (Scheme 2) and are in competition with the reaction of 2- and 3-RO$_2$ with HO$_2$ leading to the formation of the corresponding hydroperoxides, 2-ROOH and 3-ROOH. In order to estimate the 1,5 H-shift rates, we compare [2-ROOH] and [3-ROOH] at varied [HO$_2$]. Assuming that the rate coefficients for the reaction of HO$_2$ with 2- and 3-RO$_2$ are
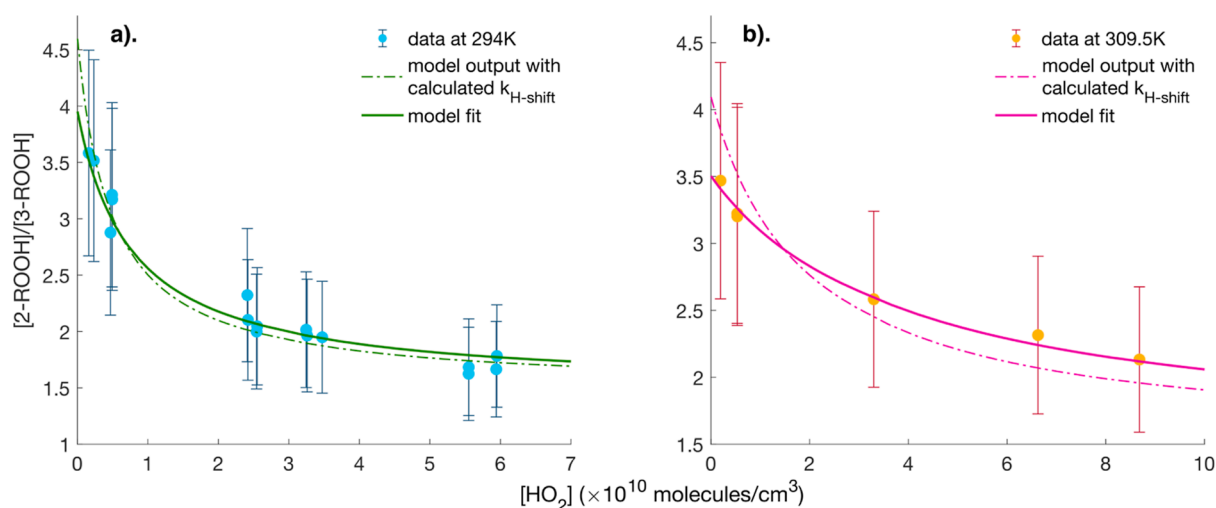
**Figure 4.** [2-ROOH]/[3-ROOH] vs [HO$_2$] at (a) ambient temperature (294 K) and (b) high temperature (309.5 K). The solid lines represent the optimized model fit to the data. The dashed lines represent the model output based on calculated H-shift rate coefficients. The uncertainties in the data are dominated by common systematic errors as detailed in Section S6 ($\sim$25% for concentration ratios and $\sim$17% for [HO$_2$]).

**Table 2. H-Shift Rate Coefficients (in s$^{-1}$) of Simple 2-EE Peroxy Radicals from Calculations and Experiments**[a]

| | | Peroxy Radicals | | |
| | | 2-RO$_2$ | 3-RO$_2$ | |
| Temperature | Method | 1,5 H-shift | 1,5 H-shift | 1,6 H-shift |
|---|---|---|---|---|
| 294K | Theory | 0.083 | 0.045 | 0.21 |
| | Experiment | 0.13 $\pm$ 0.10 | 0.13 $\pm$ 0.10 | 0.21 $\pm$ 0.13 |
| 309.5K | Theory | 0.26 | 0.14 | 0.57 |
| | Experiment | 0.54 $\pm$ 0.42 | 0.59 $\pm$ 0.46 | 0.67 $\pm$ 0.42 |

[a]Rate coefficients derived from experimental results shown here are applied in subsequent box model simulations described in the following sections. The hydrogen shown explicitly (in orange) is the hydrogen abstracted during the specified H-shift reaction. Derivation of uncertainties is detailed in Section S6.

the same, the ratio of the yields of 2-ROOH and 3-ROOH is equal to the ratio of the steady-state concentrations of the two RO$_2$

$$\frac{[2\text{-ROOH}]}{[3\text{-ROOH}]} = \frac{\alpha_{4a}k_{RO_2+HO_2}[2\text{-RO}_2]_{ss}[HO_2]}{\alpha_{4a}k_{RO_2+HO_2}[3\text{-RO}_2]_{ss}[HO_2]} = \frac{[2\text{-RO}_2]_{ss}}{[3\text{-RO}_2]_{ss}} \quad (3)$$

where $\alpha_{4a}$ indicates the branching fraction to ROOH formation, and the subscript "ss" indicates steady state. To derive the expression for [2-RO$_2$]$_{ss}$ and [3-RO$_2$]$_{ss}$, we start with the rate equations for [2-RO$_2$] and [3-RO$_2$] in the mechanism

$$\frac{d[2\text{-RO}_2]}{dt} = \alpha_{2\text{-RO}_2}k_{OH+2EE}[2\text{-EE}][OH]$$
$$- k_{RO_2+HO_2}[2\text{-RO}_2][HO_2]$$
$$- k_{1,5H\text{-shift},2\text{-RO}_2}[2\text{-RO}_2] \quad (4)$$

$$\frac{d[3\text{-RO}_2]}{dt} = \alpha_{3\text{-RO}_2}k_{OH+2EE}[2\text{-EE}][OH] - k_{RO_2+HO_2}$$
$$[3\text{-RO}_2][HO_2] - k_{1,5H\text{-shift},3\text{-RO}_2}[3\text{-RO}_2]$$
$$- k_{1,6H\text{-shift},3\text{-RO}_2}[3\text{-RO}_2] \quad (5)$$

where $\alpha_{2\text{-RO}_2}$ and $\alpha_{3\text{-RO}_2}$ are the branching fractions of 2-RO$_2$ and 3-RO$_2$ formation in the initiation step (Scheme 1). Assuming steady state for [2-RO$_2$] and [3-RO$_2$] then yields

$$[2\text{-RO}_2]_{ss} = \frac{\alpha_{2\text{-RO}_2}k_{OH+2EE}[2\text{-EE}][OH]}{k_{RO_2+HO_2}[HO_2] + k_{1,5H\text{-shift},2\text{-RO}_2}} \quad (6)$$

$$[3\text{-RO}_2]_{ss} =$$
$$\frac{\alpha_{3\text{-RO}_2}k_{OH+2EE}[2\text{-EE}][OH]}{k_{RO_2+HO_2}[HO_2] + k_{1,5H\text{-shift},3\text{-RO}_2} + k_{1,6H\text{-shift},3\text{-RO}_2}} \quad (7)$$

and the ratio between [2-RO$_2$]$_{ss}$ and [3-RO$_2$]$_{ss}$ equals

$$\frac{[2\text{-RO}_2]_{ss}}{[3\text{-RO}_2]_{ss}} = \frac{\alpha_{2\text{-RO}_2}}{\alpha_{3\text{-RO}_2}} \frac{k_{RO_2+HO_2}[HO_2] + k_{1,5H\text{-shift},3\text{-RO}_2} + k_{1,6H\text{-shift},3\text{-RO}_2}}{k_{RO_2+HO_2}[HO_2] + k_{1,5H\text{-shift},2\text{-RO}_2}} \quad (8)$$

Therefore, in the limit where [HO$_2$] is sufficiently high that the rate of bimolecular reactions vastly exceeds that of unimolecular H-shifts, the ratio of the yields of 2-ROOH and 3-ROOH is equal to the ratio of the branching fractions of 2-RO$_2$ and 3-RO$_2$ formation pathways, $\alpha_{2\text{-RO}_2}/\alpha_{3\text{-RO}_2}$). At lower HO$_2$ levels, the H-shift rates become significant in alternating the [2-ROOH]/[3-ROOH] ratio. Higher 3-RO$_2$ H-shift rates
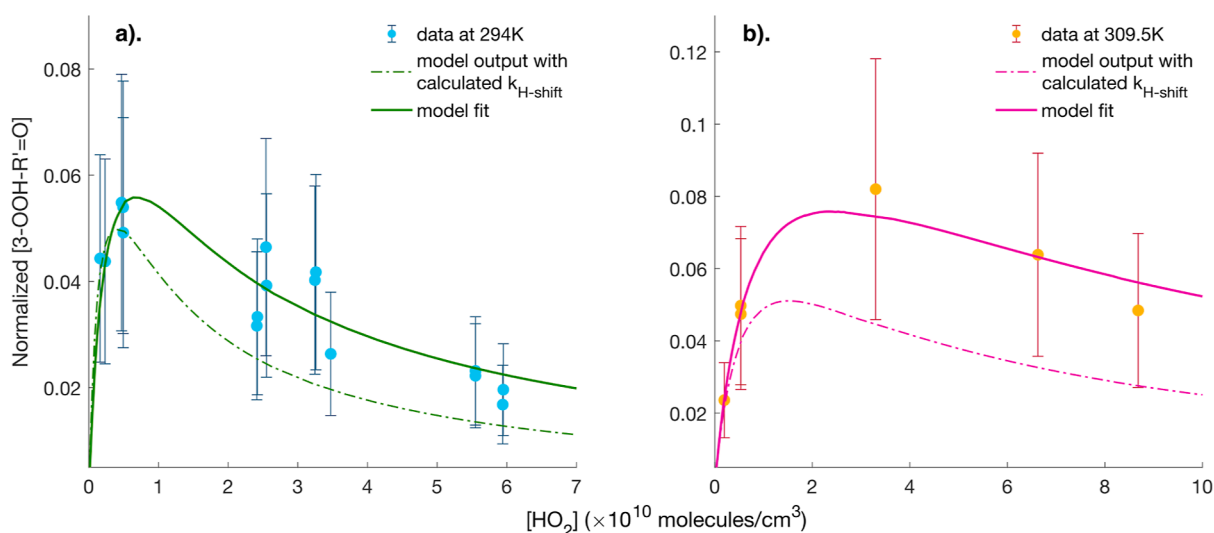
**Figure 5.** [3-OOH-R'=O] normalized by $\Delta$[2-EE] vs [HO$_2$] at (a) 294 and (b) 309.5 K. The solid lines represent the optimized model results. The dashed lines represent the model output based on calculated H-shift rate coefficients. The uncertainties in the data are dominated by common systematic errors as detailed in Section S6 (~45% for normalized concentrations and ~17% for [HO$_2$]).

lead to a higher ratio, while higher 2-RO$_2$ H-shift rates result in a lower ratio.

Based on eq 8, we adjust $\alpha_{2\text{-RO}_2}/\alpha_{3\text{-RO}_2}$ and the RO$_2$ 1,5 H-shift rate coefficients in the box model to minimize the difference between the simulation and the observations of [2-ROOH]/[3-ROOH], as shown in Figure 4. We applied our derivations of branching ratios and rate coefficients described in previous sections (RO$_2$ + HO$_2$ branching ratios and $k_{1,6\text{H-shift,3-RO}_2}$) in the simulations. This analysis suggests that the ratio between 2-RO$_2$ and 3-RO$_2$ formation from the OH + 2-EE reaction is 1.5 ± 0.4, which is in good agreement with the structure–activity relationship predictions (~1.3).[47,63,64] From the best fit of the box model to the experimental observations, we estimate the 1,5 H-shift rate coefficient of 2-RO$_2$ to be 0.13 ± 0.10 s$^{-1}$ at 294 K and 0.54 ± 0.42 s$^{-1}$ at 309.5 K, while that of 3-RO$_2$ to be 0.13 ± 0.10 s$^{-1}$ at 294 K and 0.59 ± 0.46 s$^{-1}$ at 309.5 K. These values are well within the factor-of-5 uncertainty of the MC-TST H-shift rate coefficients (see Table 2). The 1,5 H-shift rates are estimated to increase by approximately a factor of 4 with a temperature increase of ~15 K.

The estimated H-shift rates of 2- and 3-RO$_2$ are listed in Table 2. The 1,5 H-shifts of 2-EE RO$_2$ are faster than the similar 1,5 H-shift process of RO$_2$ from alkane and ketone compounds likely due to a reduction in the barrier for hydrogen abstraction alpha to the ether.[4,6,65] Similarly, due to the presence of the −OH group, the 1,6 H-shift of 3-RO$_2$ is faster than its 1,5 H-shift despite a less favorable TS geometry (seven vs six-membered ring). The higher reaction barrier for the 1,5 H-shifts also increases its temperature sensitivity compared to the 1,6 H-shift (four times vs three times increase at high temperature).[6,52]

*3.2.4. H-Shift Rates of Peroxy Radicals 2-OO-3-ROOH and 3-OO-2-ROOH.* The change in the yields of 3-OOH-R'=O at different HO$_2$ concentrations is sensitive to the H-shift rates of the second-generation peroxy radicals 2-OO-3-ROOH and 3-OO-2-ROOH. Recall that the compound 3-OOH-R'=O is formed through bimolecular chemistry of 2-OO-3-ROOH (Scheme 4). The reaction with NO/HO$_2$ produces the alkoxy radical 2-O-3-ROOH, which then decomposes to form 3-OOH-R'=O. The yield of 3-OOH-R'=O is directly constrained by the competition between H-shifts and bimolecular pathways of

2-OO-3-ROOH. It is also constrained by the competition between H-shifts and bimolecular reactions of 2-RO$_2$ and 3-RO$_2$, as well as the H-shift rates of 3-OO-2-ROOH, all of which control the yields of and the equilibrium between the two hydroperoxy RO$_2$. Thus, 3-OOH-R'=O is expected to have low yield at both extremely high and low [HO$_2$]. At high [HO$_2$], less 2-OO-3-ROOH is formed through H-shift processes due to competition with the HO$_2$ reaction, while at a low HO$_2$ level, 2-OO-3-ROOH preferentially undergoes a H-shift rather than forming the intermediate alkoxy radical.
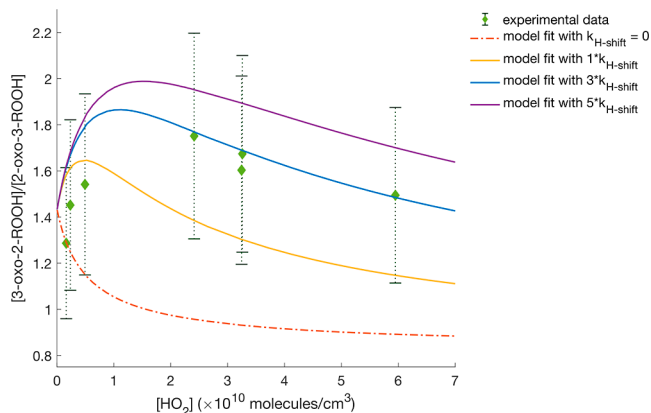
Shown in Figure 5 is [3-OOH-R'=O] normalized by the amount of 2-EE oxidized ($\Delta$[2-EE]) as a function of [HO$_2$]. With knowledge of 2-RO$_2$ and 3-RO$_2$ reaction rates and product branching ratios from previous sections, we optimize the H-shift rate coefficients for the two hydroperoxy RO$_2$ in the box model (Scheme 2) by minimizing the difference between the measured and simulated 3-OOH-R'=O yield as a function of [HO$_2$]. For the bimolecular reaction 2-OO-3-ROOH/3-OO-2-ROOH + HO$_2$, we evaluate the rate coefficients based on studies by Wennberg et al.[19] and Jenkin et al.[46] and adopt the products branching ratios from the study on methyl vinyl ether RO$_2$, a similarly multifunctional oxygenated RO$_2$ by Praske et al.[51] We provide our estimates (using the box model) for the H-shift rate coefficients for the two RO$_2$ in Table 3. We estimate that the H-shift rates increase by around a factor of 2 between 294 and 309.5 K. However, given the large uncertainties underlying our measurements (see Section S6 for detailed description of uncertainty analysis), this estimate is highly uncertain.

Given the experimental constraints, we are unable to determine stereoisomer-specific H-shift rates for the hydroperoxy RO$_2$ (like those in Scheme 2) as all our detectable products only possess one chiral center and cannot be separated on the column. Our MC-TST calculations show that there can be major differences in the H-shift rates for different diastereomers of the same peroxy and alkoxy structural radicals, as shown in Schemes 2 and 4. In some cases, such differences can be attributed to the differences in the hydrogen bonding stabilization of reactants and TSs, but such clear reasons are not always available.[3,16,37] The variation in the H-shift rates of different stereoisomers of the same radical may lead to the

enhancement of specific diastereomers of certain SOA precursors, such as the epoxide in 2-EE system, which may subsequently influence their transformation in the atmosphere and the properties of formed SOA.[37]

*3.2.5. Formation of 3-oxo-2-ROOH and 2-oxo-3-ROOH.* We partially constrain the formation pathways of major autoxidation products, the ketohydroperoxides 3-oxo-2-ROOH and 2-oxo-3-ROOH (Scheme 2), from the ratio of their yields, [3-oxo-2-ROOH]/[2-oxo-3-ROOH]. Measuring the yields of 3-oxo-2-ROOH and 2-oxo-3-ROOH are challenging, however, due to their low volatilities. The vapor pressure of the two compounds estimated by the EVAPORATION method[66] is on the order of $10^{-7}$ atm at room temperature. As a result of the low volatility, these compounds are expected to deposit significantly onto the surfaces of the chamber and the instrument. In addition to vapor-wall loss, since they eluted from the column at the highest temperature, the ketohydroperoxides are also more susceptible to losses in the column as they may undergo thermolysis at the elevated temperature required to transmit them.[67,68] As a result, we observe a low GC transmission rate of 25−30% for the $m/z$ 221 compounds. We are also unable to isolate the fractional losses of the individual isomers from our data.

Despite the difficulties in quantifying the two hydroperoxides, we do observe a trend in the ratio of their detected yields ([3-oxo-2-ROOH]/[2-oxo-3-ROOH]) as a function of [HO$_2$]. We estimate the ratio by calculating the ratio between the areas of GC peaks for the two compounds. The ratio determined from GC peak integration is likely biased low since according to our GC peak assignment, 3-oxo-2-ROOH elutes later than 2-oxo-3-ROOH and is thereby likely subject to more losses due to surface contact and potential chemical conversions in the column. In Figure 6, we show the relationship between [3-oxo-2-ROOH]/[2-oxo-3-ROOH] and [HO$_2$], where the green markers represent the ratio estimated from the experimental data. The ratio is higher at moderate HO$_2$ levels and decreases at both high and low HO$_2$ levels. This feature may arise due to another pathway that produces 3-oxo-2-ROOH in addition to

the reactions of 2-OO-3-ROOH and 3-OO-2-ROOH: the 1,5 H-shift of the 2-OO-3-ROH peroxy radical (see Scheme 4). The radical 2-OO-3-ROH is formed by isomerization of the alkoxy radical 3-O-2-ROOH, which is produced from bimolecular reactions of 3-OO-2-ROOH.

We also show in Figure 6 the ratio of [3-oxo-2-ROOH]/[2-oxo-3-ROOH] from model results with the 1,5 H-shift rate coefficient of 2-OO-3-ROH being set to 0, the calculated value, triple the calculated value, and five times the calculated value. Without the H-shift reaction, the ratio of product yields at high [HO$_2$] remains low and close to [3-OO-2-ROOH]/[2-OO-3-ROOH] at equilibrium since the bimolecular reactions of the two hydroperoxy RO$_2$ are the major source of the compounds. As the HO$_2$ level decreases, the ratio increases as the source of 3-oxo-2-ROOH shifts to the more abundant 2-OO-3-ROOH radical. When we turn on the H-shift reaction of 2-OO-3-ROOH radical, we observe an increase in [3-oxo-2-ROOH]/[2-oxo-3-ROOH]. This pathway provides an extra source for 3-oxo-2-ROOH, and, similar to 3-OOH-R'=O, produces larger amounts of 3-oxo-2-ROOH at moderate [HO$_2$] and smaller amounts at high and low [HO$_2$]. We notice that the ratios modeled from various H-shift rates converge to the same value (~1.43) at low [HO$_2$], where the production of the two ketohydroperoxides is dominated by the H-shift reactions of 2-OO-3-ROOH and 3-OO-2-ROOH. It also demonstrates that the additional formation of 3-oxo-2-ROOH arising from the 1,5 H-shift of 2-OO-3-ROH being assessed here requires a bimolecular reaction with HO$_2$, which does not occur at very low [HO$_2$]. The ratio between the two products at low [HO$_2$] is mainly determined by the equilibrium between and the H-shift rates of the two hydroperoxy RO$_2$. Thus, we expect that a better measurement of this ratio can provide another constraint for the unimolecular pathways of the two RO$_2$.
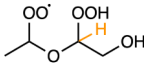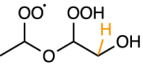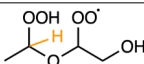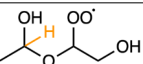
As we increase the 1,5 H-shift rate coefficient of 2-OO-3-ROH in the model, the yield of 3-oxo-2-ROOH relative to that of 2-oxo-3-ROOH peaks at greater [HO$_2$], and the modeled trend of the ratio between the two products becomes more consistent with the experimental results. The best simulation, though by no means perfect given the bias and large uncertainties in relevant parameters, occurs for H-shift rates ~3 times faster than calculated.

## 4. CONCLUSIONS

The RO$_2$ formed in the oxidation of 2-EE undergoes efficient autoxidation through intramolecular H-shift processes to produce low-volatility products and potential SOA precursors. Based on our calculations and estimations of the H-shift rate coefficients of 2-EE RO$_2$ (Tables 2 and 3), many of the H-shift reactions may occur at rates of 0.1 s$^{-1}$ or faster, corresponding to a RO$_2$ bimolecular lifetime at 10 s or shorter. We may expect that the H-shift reactions of the substrate outrun its biomolecular chemistry when the NO concentrations are ~0.5 ppb or lower on warm summer afternoons.

It is likely that other glycol ether compounds will also generate substantial yields of hydroperoxide and carbonyl-rich low-volatility autoxidation products under similar atmospheric conditions. The more carbon and oxygen-rich glycol ether substrates are likely to produce autoxidation products with extremely low vapor pressures, which readily contribute to SOA formation. The glycol ethers with longer carbon chains [such as 2-(2-ethoxyethoxy)ethanol, also known as Carbitol] may undergo consecutive H-shifts, creating new QOOH centers on the carbon backbone and increasingly oxygenated RO$_2$ to



**Figure 6.** [3-oxo-2-ROOH]/[2-oxo-3-ROOH] vs [HO$_2$] at ambient temperature (294 K). The results at high temperature (309.5 K) are shown in Figure S6 in Section S7.3. The data (in green markers) are from experiments at 294 K. The orange dashed line is the result from model run without the 1,5 H-shift reaction of 2-OO-3-ROOH radical, and the solid lines are results from model run with the MC-TST caluated 1,5 H-shift rate coefficient of 2-OO-3-ROOH scaled by factors of one (yellow), three (blue), and five (purple). The uncertainties in the data are dominated by common systematic errors, as detailed in Section S6 (~25% for concentration ratios and ~17% for [HO$_2$]).

**Table 3. H-Shift Rate Coefficients (in $s^{-1}$) of Multifunctional 2-EE Peroxy Radicals from Calculations and Experiments[b]**

| | | | Peroxy Radicals | |
| | | | 3-OO-2-ROOH | |
| | | |  |  |
| Temperature | Method | Stereoisomer | 1,5 H-shift | 1,6 H-shift |
| 294K | Theory | R, S | 0.0095 | 0.015 |
| | | S, S | 0.049 | 0.15 |
| | Experiment | | $0.047 + 0.059/ - 0.043$ | $0.12 + 0.15/ - 0.11$ |
| 309.5K | Theory | R, S | 0.034 | 0.055 |
| | | S, S | 0.15 | 0.38 |
| | Experiment | | $0.091 + 0.12/ - 0.084$ | $0.23 + 0.29/ - 0.21$ |
| | | | Peroxy Radicals | |
| | | | 2-OO-3-ROOH | 2-OO-3-ROH |
| | | |  |  |
| Temperature | Method | Stereoisomer | 1,5 H-shift | 1,5 H-shift |
| 294K | Theory | R, S | 0.064 | 0.090 |
| | | S, S | 0.022 | 0.22 |
| | Experiment | | $0.050 + 0.064/ - 0.046$ | $\sim 0.57$ |
| 309.5K | Theory | R, S | 0.19 | 0.30 |
| | | S, S | 0.082 | 0.66 |
| | Experiment | | $0.11 + 0.14/ - 0.10$ | — [a] |

[a]We refrain from providing an estimate for the 1,5 H-shift rate coefficient of 2-OO-3-ROH at high temperature as there is major divergence between the model simulation and experimental observations. See Section S7.3 for more details. [b]Rate coefficients derived from experimental results are applied in box model simulations. The hydrogen shown explicitly (in orange) is the one being abstracted during the specified H-shift reaction. Derivation of uncertainties is detailed in Section S6.

produce HOMs. This chemistry may explain the higher SOA yields observed for several glycol ether and ether compounds under $NO_x$-free conditions compared to $NO_x$-present conditions.[12,21,69]

As a result of successful policies to reduce emissions of $NO_x$ and fossil fuel VOCs in urban areas, both the chemical state and major VOC source of the modern urban atmosphere have been changing.[3,9,11] As VCPs become a major source of urban VOC emission, it is increasingly important to understand the autoxidation chemistry of those compounds to fill our knowledge gap regarding SOA growth and new particle formation in the low $NO_x$ environment. Since many VCPs such as glycol ethers are more oxygenated and functionalized than fossil fuel hydrocarbons, H-shift rates of VCP $RO_2$ are likely higher due to activation of the C—H bonds by the substituents, which lowers the barrier height for the H-shift.[6,53] Further investigations on the photochemical pathways of VCP compounds, especially their autoxidation chemistry, are essential for understanding the impact of these emissions on air quality.

## ASSOCIATED CONTENT

**Data Availability Statement**

Output files of the relevant quantum chemical calculations including xyz-geometries of the optimized structures are available online at: https://erda.ku.dk/archives/2318039e7505e595871642ff1529f42b/published-archive.html. Mechanism files of 2-EE photo-oxidation used in the box model are available at: https://doi.org/10.22002/q0x9c-6kr07.

**Supporting Information**

The Supporting Information is available free of charge at https://pubs.acs.org/doi/10.1021/acs.jpca.3c04456.

> Full mechanism of 2-EE photo-oxidation by OH; further details about experimental methods and instrumental calibration; methods of calculating secondary losses of products; experimental conditions and results; estimations of uncertainties; and additional results (PDF)

## AUTHOR INFORMATION

**Corresponding Author**

> **Paul O. Wennberg** — *Division of Geological and Planetary Sciences, California Institute of Technology, Pasadena, California 91125, United States; Division of Engineering and Applied Science, California Institute of Technology, Pasadena, California 91125, United States;* ⓞ orcid.org/0000-0002-6126-3854; Phone: +1 626 395 2447; Email: wennberg@caltech.edu

**Authors**

> **Hongmin Yu** — *Division of Geological and Planetary Sciences, California Institute of Technology, Pasadena, California 91125, United States;* ⓞ orcid.org/0000-0001-5099-3950
>
> **Kristian H. Møller** — *Department of Chemistry, University of Copenhagen, Copenhagen Ø DK-2100, Denmark;* ⓞ orcid.org/0000-0001-8070-8516
>
> **Reina S. Buenconsejo** — *Division of Chemistry and Chemical Engineering, California Institute of Technology, Pasadena, California 91125, United States*

**John D. Crounse** − *Division of Geological and Planetary Sciences, California Institute of Technology, Pasadena, California 91125, United States;* ⓞ orcid.org/0000-0001-5443-729X

**Henrik G. Kjaergaard** − *Department of Chemistry, University of Copenhagen, Copenhagen Ø DK-2100, Denmark;* ⓞ orcid.org/0000-0002-7275-8297

■ **REFERENCES**

(1) Seinfeld, J. H.; Pandis, S. N. *Atmospheric Chemistry and Physics: from Air Pollution to Climate Change*, 3rd ed.; John Wiley Sons, Inc.: Hoboken, NJ, 2016.

(2) Kroll, J. H.; Seinfeld, J. H. Chemistry of secondary organic aerosol: Formation and evolution of low-volatility organics in the atmosphere. *Atmos. Environ.* **2008**, *42*, 3593−3624.

(3) Praske, E.; Otkjær, R. V.; Crounse, J. D.; Hethcox, J. C.; Stoltz, B. M.; Kjaergaard, H. G.; Wennberg, P. O. Atmospheric autoxidation is increasingly important in urban and suburban North America. *Proc. Natl. Acad. Sci. U.S.A.* **2018**, *115*, 64−69.

(4) Crounse, J. D.; Nielsen, L. B.; Jørgensen, S.; Kjaergaard, H. G.; Wennberg, P. O. Autoxidation of organic compounds in the atmosphere. *J. Phys. Chem. Lett.* **2013**, *4*, 3513−3520.

(5) Crounse, J. D.; Paulot, F.; Kjaergaard, H. G.; Wennberg, P. O. Peroxy radical isomerization in the oxidation of isoprene. *Phys. Chem. Chem. Phys.* **2011**, *13*, 13607−13613.

(6) Bianchi, F.; Kurtén, T.; Riva, M.; Mohr, C.; Rissanen, M. P.; Roldin, P.; Berndt, T.; Crounse, J. D.; Wennberg, P. O.; Mentel, T. F.; et al. Highly Oxygenated Organic Molecules (HOM) from Gas-Phase Autoxidation Involving Peroxy Radicals: A Key Contributor to Atmospheric Aerosol. *Chem. Rev.* **2019**, *119*, 3472−3509.

(7) Ehn, M.; Berndt, T.; Wildt, J.; Mentel, T. Highly Oxygenated Molecules from Atmospheric Autoxidation of Hydrocarbons: A Prominent Challenge for Chemical Kinetics Studies. *Int. J. Chem. Kinet.* **2017**, *49*, 821−831.

(8) Russell, A. R.; Valin, L. C.; Cohen, R. C. Trends in OMI NO$_2$ observations over the United States: effects of emission control technology and the economic recession. *Atmos. Chem. Phys.* **2012**, *12*, 12197−12209.

(9) McDonald, B. C.; De Gouw, J. A.; Gilman, J. B.; Jathar, S. H.; Akherati, A.; Cappa, C. D.; Jimenez, J. L.; Lee-Taylor, J.; Hayes, P. L.; McKeen, S. A.; et al. Volatile chemical products emerging as largest petrochemical source of urban organic emissions. *Science* **2018**, *359*, 760−764.

(10) Khare, P.; Gentner, D. R. Considering the future of anthropogenic gas-phase organic compound emissions and the increasing influence of non-combustion sources on urban air quality. *Atmos. Chem. Phys.* **2018**, *18*, 5391−5413.

(11) Gkatzelis, G. I.; Coggon, M. M.; McDonald, B. C.; Peischl, J.; Gilman, J. B.; Aikin, K. C.; Robinson, M. A.; Canonaco, F.; Prevot, A. S.;

Trainer, M.; et al. Observations Confirm that Volatile Chemical Products Are a Major Source of Petrochemical Emissions in U.S. Cities. *Environ. Sci. Technol.* **2021**, *55*, 4332−4343.

(12) Li, W.; Li, L.; Chen, C. l.; Kacarab, M.; Peng, W.; Price, D.; Xu, J.; Cocker, D. R. Potential of select intermediate-volatility organic compounds and consumer products for secondary organic aerosol and ozone formation under relevant urban conditions. *Atmos. Environ.* **2018**, *178*, 109−117.

(13) Humes, M. B.; Wang, M.; Kim, S.; Machesky, J. E.; Gentner, D. R.; Robinson, A. L.; Donahue, N. M.; Presto, A. A. Limited Secondary Organic Aerosol Production from Acyclic Oxygenated Volatile Chemical Products. *Environ. Sci. Technol.* **2022**, *56*, 4806−4815.

(14) Pennington, E. A.; Seltzer, K. M.; Murphy, B. N.; Qin, M.; Seinfeld, J. H.; Pye, H. O. Modeling secondary organic aerosol formation from volatile chemical products. *Atmos. Chem. Phys.* **2021**, *21*, 18247−18261.

(15) Seltzer, K. M.; Murphy, B. N.; Pennington, E. A.; Allen, C.; Talgo, K.; Pye, H. O. Volatile Chemical Product Enhancements to Criteria Pollutants in the United States. *Environ. Sci. Technol.* **2022**, *56*, 6905−6913.

(16) Xu, L.; Møller, K. H.; Crounse, J. D.; Otkjær, R. V.; Kjaergaard, H. G.; Wennberg, P. O. Unimolecular Reactions of Peroxy Radicals Formed in the Oxidation of $\alpha$-Pinene and $\beta$-Pinene by Hydroxyl Radicals. *J. Phys. Chem. A* **2019**, *123*, 1661−1674.

(17) Wang, Y.; Mehra, A.; Krechmer, J. E.; Yang, G.; Hu, X.; Lu, Y.; Lambe, A.; Canagaratna, M.; Chen, J.; Worsnop, D.; et al. Oxygenated products formed from OH-initiated reactions of trimethylbenzene: Autoxidation and accretion. *Atmos. Chem. Phys.* **2020**, *20*, 9563−9579.

(18) Berndt, T.; Richters, S.; Jokinen, T.; Hyttinen, N.; Kurtén, T.; Otkjær, R. V.; Kjaergaard, H. G.; Stratmann, F.; Herrmann, H.; Sipilä, M.; et al. Hydroxyl radical-induced formation of highly oxidized organic compounds. *Nat. Commun.* **2016**, *7*, 13677.

(19) Wennberg, P. O.; Bates, K. H.; Crounse, J. D.; Dodson, L. G.; McVay, R. C.; Mertens, L. A.; Nguyen, T. B.; Praske, E.; Schwantes, R. H.; Smarte, M. D.; et al. Gas-Phase Reactions of Isoprene and Its Major Oxidation Products. *Chem. Rev.* **2018**, *118*, 3337−3390.

(20) Pagonis, D.; Algrim, L. B.; Price, D. J.; Day, D. A.; Handschy, A. V.; Stark, H.; Miller, S. L.; De Gouw, J. A.; Jimenez, J. L.; Ziemann, P. J. Autoxidation of Limonene Emitted in a University Art Museum. *Environ. Sci. Technol. Lett.* **2019**, *6*, 520−524.

(21) Li, L.; Cocker, D. R. Molecular structure impacts on secondary organic aerosol formation from glycol ethers. *Atmos. Environ.* **2018**, *180*, 206−215.

(22) Singer, B. C.; Destaillats, H.; Hodgson, A. T.; Nazaroff, W. W. Cleaning products and air fresheners: Emissions and resulting concentrations of glycol ethers and terpenoids. *Indoor Air* **2006**, *16*, 179−191.

(23) Fromme, H.; Nitschke, L.; Boehmer, S.; Kiranoglu, M.; Göen, T. Exposure of German residents to ethylene and propylene glycol ethers in general and after cleaning scenarios. *Chemosphere* **2013**, *90*, 2714−2721.

(24) Võ, U. U. T.; Morris, M. P. Nonvolatile, semivolatile, or volatile: Redefining volatile for volatile organic compounds. *J. Air Waste Manage. Assoc.* **2014**, *64*, 661−669.

(25) Colmenar, I.; Salgado, S.; Martín, P.; Aranda, I.; Tapia, A.; Cabañas, B. Tropospheric reactivity of 2-ethoxyethanol with OH and NO3 radicals and Cl atoms. Kinetic and mechanistic study. *Atmos. Environ.* **2020**, *224*, 117367.

(26) Espada, C.; Shepson, P. B. The production of organic nitrates from atmospheric oxidation of ethers and glycol ethers. *Int. J. Chem. Kinet.* **2005**, *37*, 686−699.

(27) Lopes, M.; Serrano, L.; Ribeiro, I.; Cascão, P.; Pires, N.; Rafael, S.; Tarelho, L.; Monteiro, A.; Nunes, T.; Evtyugina, M.; et al. Emissions characterization from EURO 5 diesel/biodiesel passenger car operating under the new European driving cycle. *Atmos. Environ.* **2014**, *84*, 339−348.

(28) Aschmann, S. M.; Atkinson, R. Kinetics of the gas-phase reactions of the OH radical with selected glycol ethers, glycols, and alcohols. *Int. J. Chem. Kinet.* **1998**, *30*, 533−540.

(29) Vasquez, K. T.; Allen, H. M.; Crounse, J. D.; Praske, E.; Xu, L.; Noelscher, A. C.; Wennberg, P. O. Low-pressure gas chromatography with chemical ionization mass spectrometry for quantification of multifunctional organic compounds in the atmosphere. *Atmos. Meas. Tech* **2018**, *11*, 6815−6832.

(30) Crounse, J. D.; McKinney, K. A.; Kwan, A. J.; Wennberg, P. O. Measurement of gas-phase hydroperoxides by chemical ionization mass spectrometry. *Anal. Chem.* **2006**, *78*, 6726−6732.

(31) Su, T.; Chesnavich, W. J. Parametrization of the ion-polar molecule collision rate constant by trajectory calculations. *J. Chem. Phys.* **1982**, *76*, 5183−5185.

(32) Garden, A. L.; Paulot, F.; Crounse, J. D.; Maxwell-Cameron, I. J.; Wennberg, P. O.; Kjaergaard, H. G. Calculation of conformationally weighted dipole moments useful in ion−molecule collision rate estimates. *Chem. Phys. Lett.* **2009**, *474*, 45−50.

(33) Murphy, S. E.; Crounse, J. D.; Møller, K. H.; Rezgui, S. P.; Hafeman, N. J.; Park, J.; Kjaergaard, H. G.; Stoltz, B. M.; Wennberg, P. O. Accretion product formation in the self-reaction of ethene-derived hydroxy peroxy radicals. *Environ. Sci.: Atmos.* **2023**, *3*, 882−893.

(34) Vereecken, L.; Peeters, J. A structure-activity relationship for the rate coefficient of H-migration in substituted alkoxy radicals. *Phys. Chem. Chem. Phys.* **2010**, *12*, 12608−12620.

(35) Møller, K. H.; Otkjær, R. V.; Hyttinen, N.; Kurtén, T.; Kjaergaard, H. G. Cost-Effective Implementation of Multiconformer Transition State Theory for Peroxy Radical Hydrogen Shift Reactions. *J. Phys. Chem. A* **2016**, *120*, 10072−10087.

(36) Møller, K. H.; Bates, K. H.; Kjaergaard, H. G. The Importance of Peroxy Radical Hydrogen-Shift Reactions in Atmospheric Isoprene Oxidation. *J. Phys. Chem. A* **2019**, *123*, 920−932.

(37) Møller, K. H.; Praske, E.; Xu, L.; Crounse, J. D.; Wennberg, P. O.; Kjaergaard, H. G. Stereoselectivity in Atmospheric Autoxidation. *J. Phys. Chem. Lett.* **2019**, *10*, 6260−6266.

(38) Zhao, Q.; Møller, K. H.; Chen, J.; Kjaergaard, H. G. Cost-Effective Implementation of Multiconformer Transition State Theory for Alkoxy Radical Unimolecular Reactions. *J. Phys. Chem. A* **2022**, *126*, 6483−6494.

(39) Halgren, T. A. Merck molecular force field. I. Basis, form, scope, parameterization, and performance of MMFF94. *J. Comput. Chem.* **1996**, *17*, 490−519.

(40) Becke, A. D. Density-functional thermochemistry. III. The role of exact exchange. *J. Chem. Phys.* **1993**, *98*, 5648−5652.

(41) Lee, C.; Yang, W.; Parr, R. G. Development of the Colle-Salvetti correlation-energy formula into a functional of the electron density. *Phys. Rev. B: Condens. Matter Mater. Phys.* **1988**, *37*, 785−789.

(42) Chai, J. D.; Head-Gordon, M. Long-range corrected hybrid density functionals with damped atom−atom dispersion corrections. *Phys. Chem. Chem. Phys.* **2008**, *10*, 6615−6620.

(43) Werner, H. J.; Knizia, G.; Manby, F. R. Explicitly correlated coupled cluster methods with pair-specific geminals. *Mol. Phys.* **2011**, *109*, 407−417.

(44) Werner, H. J.; Knowles, P. J.; Knizia, G.; Manby, F. R.; Schütz, M. Molpro: a general-purpose quantum chemistry program package. *Wiley Interdiscip. Rev.: Comput. Mol. Sci.* **2012**, *2*, 242−253.

(45) Eckart, C. The Penetration of a Potential Barrier by Electrons. *Phys. Rev.* **1930**, *35*, 1303−1309.

(46) Jenkin, M. E.; Valorso, R.; Aumont, B.; Rickard, A. R. Estimation of rate coefficients and branching ratios for reactions of organic peroxy radicals for use in automated mechanism construction. *Atmos. Chem. Phys.* **2019**, *19*, 7691−7717.

(47) Stemmler, K.; Mengon, W.; Kerr, J. A. OH radical initiated photooxidation of 2-ethoxyethanol under laboratory conditions related to the troposphere: Product studies and proposed mechanism. *Environ. Sci. Technol.* **1996**, *30*, 3385−3391.

(48) Calvert, J. G.; Mellouki, A.; Orlando, J. J.; Pilling, M. J.; Wallington, T. J. *The Mechanisms of Atmospheric Oxidation of the Oxygenates*; Oxford University Press, Inc., 2011.

(49) Stemmler, K.; Kinnison, D. J.; Kerr, J. A. Room temperature rate coefficients for the reactions of oh radicals with some monoethylene glycol monoalkyl ethers. *J. Phys. Chem.* **1996**, *100*, 2114−2116.

(50) Ziemann, P. J. Effects of molecular structure on the chemistry of aerosol formation from the OH-radical-initiated oxidation of alkanes and alkenes. *Int. Rev. Phys. Chem.* **2011**, *30*, 161−195.

(51) Praske, E.; Crounse, J. D.; Bates, K. H.; Kurtén, T.; Kjaergaard, H. G.; Wennberg, P. O. Atmospheric fate of methyl vinyl ketone: Peroxy radical reactions with NO and HO2. *J. Phys. Chem. A* **2015**, *119*, 4562−4572.

(52) Orlando, J. J.; Tyndall, G. S. Laboratory studies of organic peroxy radical chemistry: an overview with emphasis on recent issues of atmospheric significance. *Chem. Soc. Rev.* **2012**, *41*, 6294−6317.

(53) Jørgensen, S.; Knap, H. C.; Otkjær, R. V.; Jensen, A. M.; Kjeldsen, M. L.; Wennberg, P. O.; Kjaergaard, H. G. Rapid Hydrogen Shift Scrambling in Hydroperoxy-Substituted Organic Peroxy Radicals. *J. Phys. Chem. A* **2016**, *120*, 266−275.

(54) Knap, H. C.; Jørgensen, S. Rapid Hydrogen Shift Reactions in Acyl Peroxy Radicals. *J. Phys. Chem. A* **2017**, *121*, 1470−1479.

(55) Praske, E.; Otkjær, R. V.; Crounse, J. D.; Hethcox, J. C.; Stoltz, B. M.; Kjaergaard, H. G.; Wennberg, P. O. Intramolecular Hydrogen Shift Chemistry of Hydroperoxy-Substituted Peroxy Radicals. *J. Phys. Chem. A* **2019**, *123*, 590−600.

(56) Eddingsaas, N. C.; VanderVelde, D. G.; Wennberg, P. O. Kinetics and Products of the Acid-Catalyzed Ring-Opening of Atmospherically Relevant Butyl Epoxy Alcohols. *J. Phys. Chem. A* **2010**, *114*, 8106−8113.

(57) Møller, K. H.; Kurtén, T.; Bates, K. H.; Thornton, J. A.; Kjaergaard, H. G. Thermalized Epoxide Formation in the Atmosphere. *J. Phys. Chem. A* **2019**, *123*, 10620−10630.

(58) Paulot, F.; Crounse, J. D.; Kjaergaard, H. G.; Kurten, A.; St Clair, J. M.; Seinfeld, J. H.; Wennberg, P. O. Unexpected Epoxide Formation in the Gas-Phase Photooxidation of Isoprene. *Science* **2009**, *325*, 730−733.

(59) D'Ambro, E. L.; Møller, K. H.; Lopez-Hilfiker, F. D.; Schobesberger, S.; Liu, J.; Shilling, J. E.; Lee, B. H.; Kjaergaard, H. G.; Thornton, J. A. Isomerization of Second-Generation Isoprene Peroxy Radicals: Epoxide Formation and Implications for Secondary Organic Aerosol Yields. *Environ. Sci. Technol.* **2017**, *51*, 4978−4987.

(60) Surratt, J. D.; Chan, A. W.; Eddingsaas, N. C.; Chan, M. N.; Loza, C. L.; Kwan, A. J.; Hersey, S. P.; Flagan, R. C.; Wennberg, P. O.; Seinfeld, J. H. Reactive intermediates revealed in secondary organic aerosol formation from isoprene. *Proc. Natl. Acad. Sci. U.S.A.* **2010**, *107*, 6640−6645.

(61) Orlando, J. J.; Tyndall, G. S.; Wallington, T. J. The Atmospheric Chemistry of Alkoxy Radicals. *Chem. Rev.* **2003**, *103*, 4657−4690.

(62) Atkinson, R. Rate constants for the atmospheric reactions of alkoxy radicals: An updated estimation method. *Atmos. Environ.* **2007**, *41*, 8468−8485.

(63) Kwok, E. S.; Atkinson, R. Estimation of hydroxyl radical reaction rate constants for gas-phase organic compounds using a structure-reactivity relationship: An update. *Atmos. Environ.* **1995**, *29*, 1685−1695.

(64) Jenkin, M. E.; Valorso, R.; Aumont, B.; Rickard, A. R.; Wallington, T. J. Estimation of rate coefficients and branching ratios for gas-phase reactions of OH with aliphatic organic compounds for use in automated mechanism construction. *Atmos. Chem. Phys.* **2018**, *18*, 9297−9328.

(65) Otkjær, R. V.; Jakobsen, H. H.; Tram, C. M.; Kjaergaard, H. G. Calculated Hydrogen Shift Rate Constants in Substituted Alkyl Peroxy Radicals. *J. Phys. Chem. A* **2018**, *122*, 8665−8673.

(66) Compernolle, S.; Ceulemans, K.; Müller, J. F. Evaporation: A new vapour pressure estimation methodfor organic molecules including non-additivity and intramolecular interactions. *Atmos. Chem. Phys.* **2011**, *11*, 9431−9450.

(67) Wang, S.; Zhao, Y.; Chan, A. W.; Yao, M.; Chen, Z.; Abbatt, J. P. Organic Peroxides in Aerosol: Key Reactive Intermediates for Multiphase Processes in the Atmosphere. *Chem. Rev.* **2023**, *123*, 1635−1679.

(68) Zhao, Z.; Yang, X.; Lee, J.; Tolentino, R.; Mayorga, R.; Zhang, W.; Zhang, H. Diverse Reactions in Highly Functionalized Organic

Aerosols during Thermal Desorption. *ACS Earth Space Chem.* **2020**, *4*, 283−296.

(69) Zhu, J.; Li, J.; Du, L. Exploring the formation potential and optical properties of secondary organic aerosol from the photo-oxidation of selected short aliphatic ethers. *J. Environ. Sci.* **2020**, *95*, 82−90.